

Robust Longitudinal-lateral Look-ahead Pursuit Path-Following Control: Fast Finite-Time Stability Guarantee

Zimao Sheng^a, Hong'an Yang^{a,*}, Shuxiang Yang^a and Zirui Yu^b

^aSchool of Mechanical Engineering, Northwestern Polytechnical University, Xi'an, Shaanxi, 710072, China

^bSchool of Artificial Intelligence, Tianjin University of Science and Technology, Tianjin, 300457, China

ARTICLE INFO

Keywords:

Robust path-following guidance law
Bounded external disturbances
Robust stability
Global random attractor

ABSTRACT

This paper addresses the challenging problem of robust path-following for fixed-wing unmanned aerial vehicles (UAVs) in complex environments with bounded external disturbances and non-smooth predefined paths. Due to the unique aerodynamic characteristics and flight constraints of fixed-wing UAVs, achieving accurate and fast stable path following remains difficult, especially in low-altitude mountainous terrains, urban landscapes, and under wind disturbances. Most existing path-following guidance laws often struggle to ensure fast stabilization under unknown bounded disturbances while maintaining sufficient robustness, and there is a lack of research on optimizing robustness for non-smooth paths under flight constraints. This paper addresses these issues by proposing a constraints-based robust path-following controller. Firstly, from the perspective of global random attractor, we innovatively introduce robustness metrics that quantify both the exponential convergence rate and the range of the ultimate attractor set. Secondly, building on these metrics, we develop a robust longitudinal-lateral look-ahead pursuit (RLLP) guidance law for fixed-wing UAVs, specifically considering the flight path angle and track angle under external disturbances. Thirdly, we also derive an optimized version (Optimal-RLLP) to enhance the robustness metrics, and elaborate on the sufficient conditions for fast finite-time stability, ensuring the guidance law achieves finite-time stability and robustness with reduced sensitivity to constrained uncertainties. The simulation results validate the proposed guidance law's feasibility, optimality and robustness under atmospheric disturbances using a high-fidelity simulation platform and provide key principle for practical deployment.

1. Introduction

1.1. Motivation

In recent years, fixed-wing unmanned aerial vehicles (UAVs) are widely used in extensive range of applications encompassing environmental monitoring[1], rescue operations[2], military reconnaissance[3], etc., primarily due to their attributes of large payload capacity, high speed, and long flight endurance. The autonomous missions execution of many fixed-wing UAVs heavily relies on predefined geometric path following [4][5][6] guidance law, which is deployed in the flight control system (FCS) and outputs the acceleration commands according to the predefined path and constraints on the vehicle's dynamics. However, due to the unique aerodynamic characteristics and flight constraints of fixed-wing UAVs, achieving robust path following in complex low-altitude mountainous terrains, urban landscapes, and under wind disturbances remains a challenging problem. The conventional path-following problem under perturbed conditions tends to impose external disturbances on the three-axis velocities, neglecting the impact on flight-path angle and track angle. Furthermore, most path-following guidance laws struggle to ensure fast stabilization under unknown bounded disturbances while maintaining a certain robustness threshold. Additionally, there is a lack of further research on how to optimally design the robustness for non-smooth paths based on the flight constraints. These

issues inspire us to design a robust constraints-based path-following controller that can achieve fast robust stability and fast finite-time stability in the case of unstructured predefined path and constrained disturbances.

1.2. Related work

Classical path-following algorithms have predominantly focused on 2D contexts[6][7][8]. In order to tackle the challenge of achieving high-robustness online 3D UAVs path-following, the primary methodologies[9] have encompassed error regulation based[10][11][12], optimal control[13][14], vector field based[15][16], and virtual target based[17][18][19] approaches.

Error regulation based method prioritizes the achievement of asymptotic convergence for positional errors. Piprek[11] decoupled the three-dimensional error model into time-varying linear models in both lateral and longitudinal planes, achieving error asymptotic stability by configuring the pole positions of the linear time-varying system (LTV) at any given moment. Isaac[10] employed the L_1 adaptive augmentation algorithm to design an adaptive feedback controller for the linearized kinematic model of UAVs by solving the Lyapunov equation under perturbed conditions, thereby guaranteeing the tuning effectiveness of the error. Takeshi[12], however, constrained the convergence surface of the tracking error by solving for high-order sliding mode variable structure control. Nevertheless, these methods struggles to guarantee a effective stable time, and model-based control is overly complex and challenging to implement into the autopilot for 3D path-following.

*Corresponding author

✉ hpShengZimao@163.com (Z. Sheng); yhongan@nwpu.edu.cn (H. Yang)

ORCID(s): 0000-0001-6067-3379 (Z. Sheng); 0000-0001-5426-0041 (H. Yang)

Yang)

Optimal control based method tends to utilize optimal control techniques to minimize both the quadratic form of tracking deviation and the quadratic form of control input over a future time horizon. Ahmed[13] employed quasi-linear parameter-varying model predictive control (ql-MPC) with time-varying semilinear characteristics to perform rolling optimization for solving the optimal strategy of a three-dimensional perturbed velocity form kinematic model, achieving robust path following under high disturbance conditions. Yang[14] designed a finite-time-horizon optimal control law for an affine kinematic model under perturbed conditions, enabling exponential convergence of path tracking deviations. However, such optimal control methods have high computational costs, making it difficult to meet the requirements for real-time path following.

Vector field based method involves designing a vector field to compel the UAV flight trajectory to follow a path formed by the intersection of multiple planes[16]. However, this method is primarily suited for relatively regular and simple paths[15] such as straight lines and arcs, and it falls short when dealing with complex path following tasks.

Compared to the aforementioned methods, due to its simplicity, the virtual target based method is more commonly used in practice[19]. In this approach, the UAV continuously approximates a virtual target point moving along a predefined path. The virtual target can be set in front of the current position and on the extension of the desired path. Its distance is related to the current tracking error. By real-time measuring position and angle errors, and correcting the attitude input of the UAV between the current position and the virtual target, the actual trajectory and the predefined path will exhibit a high degree of congruence, thereby realizing efficient path-following. This characteristic makes the algorithm suitable for following a relatively general 3D path. Zian[17] employed the L_1 guidance law in both the horizontal and vertical planes for a 3D UAV to achieve optimal path point approximation and thus path following after selecting the optimal virtual approach point, which led to the successful completion of real-flight experiments. However, this method struggles to guarantee positional and angular tracking errors, and it may not robustly and stably converge under external disturbances caused by factors such as wind fields and the movement of virtual points. Despite existing research[18] attempts to address the finite-time stability of path-following errors under wind disturbances, these methods still primarily consider relatively simple 2D particle model and the wind disturbances are mainly imposed on the impact on velocity, instead of angular rates. Additionally, they seldom take into account the input command saturation and the effectiveness of following non-smooth path.

The impact of disturbance factors, including wind field disturbances and model simplification, on the path following performance under constrained kinetic limitations, is often substantial. These disturbances directly influence the flight velocity and angular rate of UAVs. Therefore, a relatively straightforward approach is to correct the disturbance term by incorporating a compensation quantity. As a result,

Thomas[20] introduces an airspeed reference command increment according to the wind speed ratio, and the L_1 ratio and feasibility parameters are adaptively compensated in an attempt to mitigate run-away phenomena in over-wind scenarios. The authors[14][21] seeks to employ disturbance observers to dynamically compensate for the estimated disturbances, thereby bolstering the robustness of the guidance rate in the presence of wind disturbances. Similarly, compensation effects can also be applied to classical feedback controllers to address external disturbances. Souanef[22] employs feedback linearized dynamics compensation based on L_1 adaptive control for UAVs path-following controller with parametric uncertainties and external disturbances. Wu[23] proposed a robust fuzzy control scheme that employs a proportional-integral-derivative(PID) controller based on feedback linearization to compensate nonlinear deviations caused by system uncertainties and modeling parameters.

The previously mentioned efforts have yielded satisfactory performance improvements in mitigating the effects of disturbances, yet most research frameworks still rely on controllers that guarantee asymptotic convergence. Such controllers may be hard to ensure rapid convergence time and robustness metric[18]. When virtual target points are densely distributed, these controllers may find it challenging to handle disturbances and uncertainties, leading to deviations in the system's steady state. The system may exhibit oscillations and unpredictable behaviors while abrupt changes in state occur due to external disturbances such as wind fields, measurement noise, and other error sources. Furthermore, the system's path-following error is further amplified by factors such as external disturbances, if the UAV is initially far away from the desired path, the movement of virtual target points, and sharp curvatures, resulting in an inability to provide the expected following performance. Nevertheless, the above-mentioned model-based methodologies pose challenges in guaranteeing error stabilization within a finite timeframe in the presence of external perturbations.

1.3. Contribution

In this paper, we further augment the preliminary results obtained in[17] with additional in-depth analysis, deriving a robust guidance law in the presence of bounded external disturbances and non-smooth predefined path within finite-time stability guarantee, and summarize our main contributions below.

- Addressing the quantification of robust stability for perturbed nonlinear dynamic systems, we innovatively propose robustness metrics from the perspective of global random attractor—metrics that quantify both the exponential convergence rate and the range of the ultimate attractor set. This work establishes a foundation for subsequent robustness analysis of the robust longitudinal and lateral look-ahead pursuit path-following guidance law;

- To quantify and enhance the robustness of traditional look-ahead pursuit guidance laws, we further elaborate on the sufficient conditions for their fast finite-time stability. Building upon the aforementioned robustness metrics, we present a robust longitudinal and lateral look-ahead pursuit (RLLP) guidance law for fixed-wing UAVs, with specific consideration of the flight path angle and track angle under external disturbances. Additionally, we derive an optimized version of the RLLP (Optimal-RLLP) that further improves its robustness metrics. Consequently, the proposed guidance law guarantees finite-time stability, robustness, reduced sensitivity to constrained uncertainties compared to traditional asymptotic convergence controllers. Results validate the guidance law's robustness under small disturbances and its feasibility for practical deployment;
- We verify the feasibility and robustness of the RLLP guidance law based on a UAV path-following platform integrating realistic low-altitude urban scenarios, actual UAV dynamic models, aerodynamic models, and atmospheric disturbances. Through detailed analysis, we provide principles for adjusting algorithm parameters when deploying the RLLP in practical applications.

The remainder of this paper is organized as follows. After an overview in Section 1, the numerous theoretical results regarding the robustness of nonlinear perturbed systems intended for subsequent guidance law design is given in Section 2, and the perturbed model and constrained input commands, along with the problem formulation, is presented in Section 3. The proposed robust guidance law and its modified optimal version is designed in Section 4, followed by a matched autopilot design in Section 5 and simulation experiments in Section 6. Finally, we present concluding remarks and directions for future investigation in Section Conclusions and future work.

2. Preliminaries

In this section, we present several key definitions, lemmas, and theorems as essential tools for subsequent analyses.

2.1. Definitions

Definition 1. (Robust stability) For perturbed nonlinear system $\dot{y} = f(t, y) + g(t, y)$, $y \in \mathbb{R}^n$, $f(t, 0) = 0$, $f, g \in C[I \times S_H, \mathbb{R}^n]$, $S_H = \{x \mid \|x\| \leq H\}$, if $\forall \epsilon > 0$, there exists $\delta_1(\epsilon) > 0$ and $\delta_2(\epsilon) > 0$ to make $\|g(t, y)\| \leq \delta_1(\epsilon)$, $\|y(0)\| \leq \delta_2(\epsilon)$, and $\|y\| \leq \epsilon$, then the trivial solution of $\dot{y} = f(t, y) + g(t, y)$, $f(t, 0) = 0$ exhibits robust stability.

Definition 2. (Global attractor) For a dynamical system: $\dot{x}(t) = f(x(t))$, $x(t) \in \mathbb{R}^n$, where $f : \mathbb{R}^n \rightarrow \mathbb{R}^n$ is a deterministic vector field (typically Lipschitz continuous). The set A for this state $x(t)$ is defined as the global attractor if $x(t) \notin A$, then the distance between $x(t)$ and A : $\text{dist}(x(t), A) \rightarrow 0$ as $t \rightarrow \infty$; if $x(t) \in A$, then $x(t + \Delta t) \in A$ for any $\Delta t \geq 0$.

Definition 3. (Global random attractor) For a dynamical system governed by a stochastic differential equation (SDE): $\dot{x} = f(x) + d$, $x \in \mathbb{R}^n$ and d is a stochastic perturbation. Its global attractor can be regarded as the global random attractor of the SDE.

Definition 4. (Co-Lipschitz property) For function $f : X \rightarrow \mathbb{R}^m$, $X \subset \mathbb{R}^n$, if there exists $L > 0$ for any $x_1, x_2 \in X$ such that $\|f(x_1) - f(x_2)\|_2 \geq L\|x_1 - x_2\|_2$ holds, then f is referred to L -co-Lipschitz over X .

2.2. Key lemmas and theorem

Lemma 1. (Stability of matrix[24]) If A is stable, which means $\text{Res}(A) < 0$ or eigenvalue 0 corresponds to the single characteristic factor, there exists only one positive definite $P = P^T = P(A, \delta) > 0$ for any $\delta > 0$ to make:

$$P(A, \delta)A + A^T P(A, \delta) + \delta I = O \quad (1)$$

Lemma 2. (The fast finite-time stability[25]) For a nonlinear system $\dot{x}(t) = f(x(t))$ with $f(0) = 0$, $x \in \Omega \subset \mathbb{R}^n$, suppose there is a positive definite function $V(x)$ for any nonzero x satisfying

$$\dot{V}(x) + \alpha V(x) + \beta V^\gamma(x) \leq 0 \quad (2)$$

where $\alpha > 0$, $\beta > 0$ and $0 \leq \gamma < 1$. Then, the origin of system is fast finite-time stable in Ω , and the settling time, depending on the initial state $x(0) = x_0$, is given by

$$T(x_0) \leq \frac{1}{\alpha(1-\gamma)} \ln\left(1 + \frac{\alpha V^{1-\gamma}(x_0)}{\beta}\right) \quad (3)$$

Lemma 3. (The fast finite-time stability[25]) For a nonlinear system $\dot{x}(t) = f(x(t))$ with initial state $x(0) = x_0$, $f(0) = 0$, $x \in \mathbb{R}^n$, suppose there exists a positive definite function $V(x)$ for any nonzero x satisfying

$$\dot{V}(x) + \alpha V(x) - \beta V^{\frac{1}{2}}(x) \leq 0 \quad (4)$$

where $\alpha > 0$, $\beta > 0$. Then for any state $x(t)$ there exists

$$V^{\frac{1}{2}}(x(t)) \leq \frac{\beta}{\alpha} + (V^{\frac{1}{2}}(x_0) - \frac{\beta}{\alpha})e^{-\frac{\alpha}{2}t} \quad (5)$$

Proof. We define $s(t) = V^{\frac{1}{2}}(x)$, and then Eq.(4) can be transformed into

$$\dot{s}(t) + \frac{\alpha}{2}s(t) \leq \frac{\beta}{2} \quad (6)$$

The above equation can be further transformed into

$$e^{\frac{\alpha}{2}t}\dot{s}(t) + \frac{\alpha}{2}e^{\frac{\alpha}{2}t}s(t) \leq \frac{\beta}{2}e^{\frac{\alpha}{2}t} \quad (7)$$

which means

$$\frac{d}{dt}(e^{\frac{\alpha}{2}t}s(t)) \leq \frac{\beta}{2}e^{\frac{\alpha}{2}t} \quad (8)$$

Integrating both sides of the inequality in the above equation from 0 to t simultaneously, we can obtain

$$e^{\frac{\alpha}{2}t}s(t) - s(0) \leq \frac{\beta}{\alpha}(e^{\frac{\alpha}{2}t} - 1) \quad (9)$$

Therefore, the above equation can be further derived to obtain Eq.(5). Thus, the proof is completed. \square

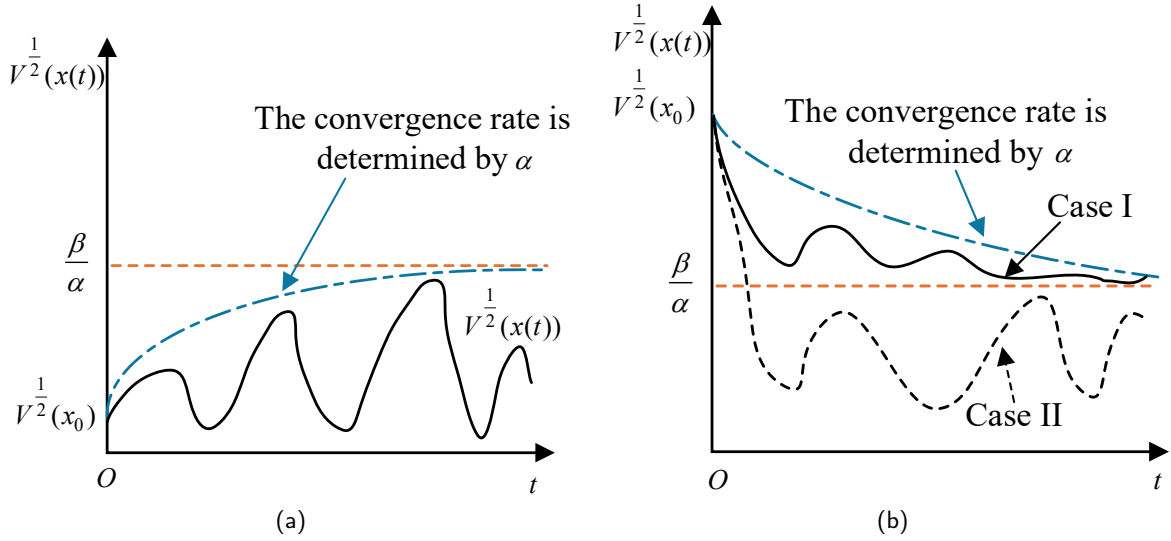


Figure 1: The curves depicting the evolution of $V^{\frac{1}{2}}(x_t)$ are presented under diverse initial values of $V^{\frac{1}{2}}(x_0)$. (a): $V^{\frac{1}{2}}(x_0) \leq \frac{\beta}{\alpha}$; (b): $V^{\frac{1}{2}}(x_0) > \frac{\beta}{\alpha}$.

Remark 1. Eq.(5) reveals a fact that, as illustrated in Figure 1, when the initial value x_0 satisfies $V^{\frac{1}{2}}(x_0) \leq \frac{\beta}{\alpha}$, $V^{\frac{1}{2}}(x(t)) \leq \frac{\beta}{\alpha}$ holds for all $t \geq t_0$. Conversely, if $V^{\frac{1}{2}}(x_0) \geq \frac{\beta}{\alpha}$, $V^{\frac{1}{2}}(x(t))$ is upper-bounded by a function that converges exponentially to $\frac{\beta}{\alpha}$ with a rate of α . As t approaches infinity, once $V^{\frac{1}{2}}(t_r) \leq \frac{\beta}{\alpha}$ is satisfied at a certain time t_r , the trajectory of $x(t)$ will remain within this region indefinitely. Consequently, it can be deduced that for any initial value $x(t_0) = x_0$, $x(t)$ will ultimately converge to the global attractor described as:

$$x(t) \in \{x | V^{\frac{1}{2}}(x) \leq \frac{\beta}{\alpha}\}, t \rightarrow \infty \quad (10)$$

It is worth noting that we generally aspire for the convergence rate α to be as large as possible. Meanwhile, a larger α also enables the scope of the random attractor, $\frac{\beta}{\alpha}$, to be minimized. On the basis of above, we introduce the following theorem as our main result:

Theorem 1. For the perturbed autonomous system $\dot{x} = f(x) + d$, where $x \in \mathbb{R}^n$, $x(t_0) = x_0$, $f(0) = 0$, and $d \in \mathbb{R}^n$ is the perturbation term satisfying $\|d\|_2 \leq L_d$. If there exists a set Ω such that when $x \in \Omega$, the following conditions hold: 1) there exists $L_f(\Omega) \geq 0$ such that $\left\| \frac{\partial f(x)}{\partial x} \right\|_2 \leq L_f(\Omega)$; 2) there exists a positive-definite matrix $P = P^T > 0$ and $\varepsilon(\Omega) > 0$ such that $\left[\frac{\partial f(x)}{\partial x} \right]^T P + P \frac{\partial f(x)}{\partial x} + \varepsilon(\Omega)I \leq 0$. Then the ultimate trajectory of the state $x(t)$, for any initial value x_0 , $x(t)$ will exponentially converge to the following global random attractor $S(\Omega)$ at least the rate of

$\varepsilon(\Omega)/\lambda_{\max}(P)$ as $t \rightarrow \infty$:

$$x(t) \rightarrow S(\Omega) = \{x : \|f(x)\|_2 \leq \frac{2L_d L_f(\Omega) \lambda_{\max}^2(P)}{\varepsilon(\Omega) \lambda_{\min}(P)}\} \quad (11)$$

Proof. Let $V(x) = f(x)^T P f(x)$ for $P = P^T > 0$ such that

$$\begin{aligned} \dot{V}(x) &= \dot{f}(x)^T P f(x) + f(x)^T P \dot{f}(x) \\ &= \dot{x}^T \left[\frac{\partial f(x)}{\partial x} \right]^T P f(x) + f(x)^T P \left[\frac{\partial f(x)}{\partial x} \right] \dot{x} \\ &= f(x)^T \left(\left[\frac{\partial f(x)}{\partial x} \right]^T P + P \frac{\partial f(x)}{\partial x} \right) f(x) \\ &\quad + d^T \left[\frac{\partial f(x)}{\partial x} \right]^T P f(x) + f(x)^T P \frac{\partial f(x)}{\partial x} d \\ &\leq -\frac{\varepsilon(\Omega)}{\lambda_{\max}(P)} V(x) + 2d^T \left[\frac{\partial f(x)}{\partial x} \right]^T P f(x) \\ &\leq -\frac{\varepsilon(\Omega)}{\lambda_{\max}(P)} V(x) + 2L_d \left\| \frac{\partial f(x)}{\partial x} \right\|_2 \|P f(x)\|_2 \\ &\leq -\frac{\varepsilon(\Omega)}{\lambda_{\max}(P)} V(x) + \frac{2L_d L_f(\Omega) \lambda_{\max}(P)}{\sqrt{\lambda_{\min}(P)}} V(x)^{\frac{1}{2}} \end{aligned} \quad (12)$$

According to the Lemma 3 and Remark 1, as $t \rightarrow \infty$,

$$V^{\frac{1}{2}}(x) \leq \frac{2L_d L_f(\Omega) \lambda_{\max}^2(P)}{\varepsilon(\Omega) \sqrt{\lambda_{\min}(P)}} \quad (13)$$

Consequently, as $t \rightarrow \infty$,

$$\|f(x)\|_2 \leq \frac{V^{\frac{1}{2}}(x)}{\sqrt{\lambda_{\min}(P)}} \leq \frac{2L_d L_f(\Omega) \lambda_{\max}^2(P)}{\varepsilon(\Omega) \lambda_{\min}(P)} \quad (14)$$

The proof is completed. \square

Theorem 1 elucidates a pivotal theoretical framework. Let Ω be a non-empty subset of the state space \mathbb{R}^n that encompasses the origin. When the Jacobian of the function $f(x)$, denoted as $J_f(x) = \partial f(x)/\partial x$, is uniformly bounded for all x within the domain Ω , and $J_f(x)$ exhibits negative definiteness throughout this region, the following property emerges for the associated dynamical system. For an autonomous dynamical system governed by the differential equation $\dot{x}(t) = f(x(t)) + d$, regardless of the chosen initial condition $x_0 \in \mathbb{R}^n$, the time-derivative of the state trajectory $f(x(t))$, will converge exponentially to the global random attractor as delineated in Eq.(11). The spatial extent of this attractor is intricately linked to two critical parameters: the supremum $L_f(\Omega)$ of the norm of the Jacobian $J_f(x)$ over the domain Ω , and the maximum eigenvalue upper bound of $J_f(x)$ under Ω . Specifically, a smaller upper bound for the ultimate attractor $\|f(x)\|_2$ can be achieved through a smaller $L_f(\Omega)$ and a larger $\varepsilon(\Omega)$.

Remark 2. According to Lemma 1, there exists a sufficient condition for the validity of condition 2) in Theorem 1, specifically: when $x \in \Omega$, the Jacobian $\partial f/\partial x$ is stable. Furthermore, a special case arises when $\Omega = \{0\}$, in this scenario, determining whether $\partial f(0)/\partial x$ satisfies conditions 1) and 2) suffices to characterize the global random attractor $S(0)$ of the perturbed system's trajectory.

Remark 2 establishes the following theoretical principle: if the Jacobian matrix $\partial f/\partial x$ of $f(x)$ is continuously bounded and stable over a region $x \in \Omega$, then the trajectory $x(t)$ of the perturbed system will exponentially converge to a global random attractor in which the fluctuation amplitude of $f(x)$ remains bounded. Notably, the extent of this attractor is governed by the eigenvalues of $\partial f/\partial x$ —larger eigenvalue magnitudes generally correspond to a smaller constrained domain, thereby enabling the system to attain a higher level of robust stability.

To minimize the upper bound of $\|f(x)\|_2$ in Eq.(11), one must ensure that the ratio $\lambda_{\max}(P)/\lambda_{\min}(P)$ is minimized and the ratio $\varepsilon(\Omega)/\lambda_{\max}(P)$ is maximized. Given that $\lambda_{\max}(P) \geq \lambda_{\min}(P)$, the ratio $\lambda_{\max}(P)/\lambda_{\min}(P)$ reaches its minimum when $\lambda_{\max}(P) = \lambda_{\min}(P) = \varepsilon_P I_n$ (where I_n denotes the identity matrix). Under this condition, when $\Omega = \{0\}$ and f is L_c -co-Lipschitz on its neighborhood, the following more specialized conclusion holds.

Theorem 2. For the perturbed autonomous system $\dot{x} = f(x) + d$, where $x \in \mathbb{R}^n, x(t_0) = x_0, f(0) = 0$, and $d \in \mathbb{R}^n$ is the perturbation term satisfying $\|d\|_2 \leq L_d$. If the following conditions hold:

- 1) there exists $L_f \geq 0$ such that $\left\| \frac{\partial f(0)}{\partial x} \right\|_2 \leq L_f$;
 - 2) f is L_c -co-Lipschitz on the neighbor of origin;
 - 3) there exists $\varepsilon > 0$ such that $\left[\frac{\partial f(0)}{\partial x} \right]^T + \frac{\partial f(0)}{\partial x} + \varepsilon I_n \leq O$.
- Then the ultimate trajectory of the state $x(t)$, for any initial value x_0 , $x(t)$ will exponentially converge to the following global random attractor $S(0)$ at least the rate of ε as $t \rightarrow \infty$:

$$x(t) \rightarrow S(0) = \{x : \|x\|_2 \leq \frac{2L_d L_f}{\varepsilon L_c}\} \quad (15)$$

Proof. Let $P = \varepsilon_P I_n > 0, \varepsilon = \varepsilon(0)/\varepsilon_P$, according to the Theorem 1 and Remark 2,

$$x(t) \rightarrow S(0) = \{x : \|f(x)\|_2 \leq \frac{2L_d L_f}{\varepsilon}\}, t \rightarrow \infty \quad (16)$$

Since f is L_c -co-Lipschitz on the neighborhood of the origin, i.e., as $t \rightarrow \infty$,

$$\|x\|_2 \leq \frac{\|f(x) - f(0)\|_2}{L_c} \leq \frac{2L_d L_f}{\varepsilon L_c} \quad (17)$$

This completes the proof. \square

Remark 3. According to Theorem 2, on the one hand, ε reflects the exponential convergence rate of the trajectory $x(t)$; on the other hand, it also characterizes the size of the global random attractor. This implies that a larger ε corresponds to a faster convergence rate and a smaller attractor size (ideally, the attractor is the origin), i.e., higher robustness. On the one hand, the robustness of this perturbed dynamical system can be defined by the index ε , which is further described as:

$$R(f) = -\lambda_{\max} \left(\left[\frac{\partial f(0)}{\partial x} \right]^T + \frac{\partial f(0)}{\partial x} \right) > 0 \quad (18)$$

On the other hand, the final attractor size caused by f can be quantified by the following indicator:

$$I(f) = \frac{L_f}{L_c} \frac{1}{R(f)} \quad (19)$$

3. Problem Formulation

This paper focuses on developing a robust path-following solution for fixed-wing UAV in the presence of disturbances such as wind fields and model simplifications. Assuming that a UAV intends to adhere to a generic, predefined reference path points denoted as

$$\mathcal{P} = \{(x_{c,i}, y_{c,i}, z_{c,i})\}_{i=1}^n \quad (20)$$

The UAV's dynamic equations of motion, while maintaining a given ground speed V_g , can be organized as[17]

$$\begin{cases} \dot{x}_p = V_g \cos \gamma \cos \chi \\ \dot{y}_p = V_g \cos \gamma \sin \chi \\ \dot{z}_p = V_g \sin \gamma \end{cases} \quad (21)$$

where (x_p, y_p, z_p) denotes the position of the UAV in the north-east-up inertial coordinate system, γ is the UAV's flight path angle and χ is the UAV's course angle.

3.1. Lateral coordinated turn

The lateral coordinated turn is a sought-after flight condition in unmanned flight by controlling the aircraft's bank angle ϕ . During a coordinated turn, the aircraft carves the turn rather than skidding laterally. From an analysis perspective, the assumption of a coordinated turn allows us to develop a simplified expression that relates course rate and bank angle. During a coordinated turn, the bank angle ϕ

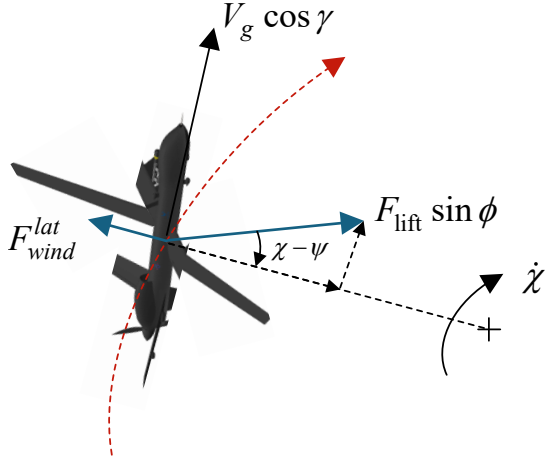


Figure 2: Free-body UAV diagram indicating forces on a UAV in a lateral coordinated turn, where F_{wind}^{lat} is the projection of the wind field force onto the lateral plane.

is set so that there is no net side force acting on the UAV. The centrifugal force acting on the UAV is equal to the summation of horizontal component of the lift force and windy force, as shown in Figure 2. Summing forces in the horizontal direction gives

$$F_{lift} \sin \phi \cos(\chi - \psi) - F_{wind}^{lat} = m(V_g \cos \gamma) \dot{\chi} \quad (22)$$

where ψ is the heading angle, F_{lift} is the lift force, F_{wind}^{lat} is the windy force projection along the lateral plane.

3.2. Longitudinal accelerating climb

To derive the dynamics for the flight-path angle, we will consider a pull-up maneuver in which the aircraft climbs along an arc. Define the two dimensional plane as the plane containing the velocity vector V_g and the vector from the center of mass of the aircraft to the instantaneous center of the circle defined by the pull-up maneuver, as shown in Figure 3. Similarly, the vertical component of the lift force has to cancel the summation of the projection of gravitational force and windy force onto the longitudinal plane to remain at a climb rate, and the centripetal force due to the pull-up maneuver is $mV_g \dot{\gamma}$. Therefore, summing the forces in the longitudinal plane gives

$$F_{lift} \cos \phi - mg \cos \gamma - F_{wind}^{lon} = mV_g \dot{\gamma} \quad (23)$$

3.3. UAV's perturbed dynamic model

The load factor is defined as the ratio of the lift force acting on an aircraft to its weight:

$$n_{lf} = \frac{F_{lift}}{mg} \quad (24)$$

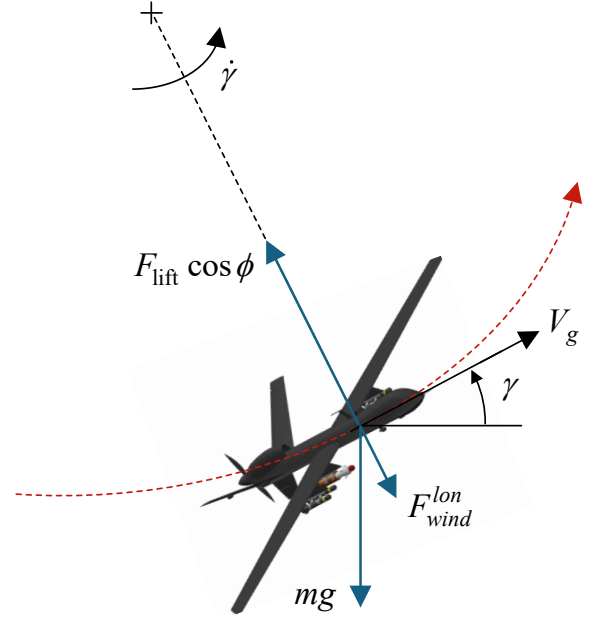


Figure 3: Free-body UAV diagram indicating forces on a UAV in a longitudinal accelerating climb, where F_{wind}^{lon} is the projection of the wind field force onto the longitudinal plane.

From a control engineering perspective, the load factor n_{lf} is a critical parameter, as it quantifies the dynamic forces experienced by the aircraft during climbing and turning maneuvers. By treating the load factor as a state variable in control systems, we can enforce command constraints within the aircraft's structural limits, ensuring operational safety and integrity. By reorganizing Eq.(22) and Eq.(23), we derive:

$$\begin{cases} \dot{\chi} = \frac{g}{V_g} \tan \phi \cos(\chi - \psi) + d_\chi \\ \dot{\gamma} = \frac{g}{V_g} (n_{lf} \cos \phi - \cos \gamma) + d_\gamma \end{cases} \quad (25)$$

where disturbance term $d = (d_\chi, d_\gamma)^T$ can be expressed as

$$\begin{cases} d_\chi = \frac{(mV_g \dot{\gamma} + F_{wind}^{lon}) \tan \phi \cos(\chi - \psi) - F_{wind}^{lat}}{mV_g \cos \gamma} \\ d_\gamma = -\frac{F_{wind}^{lon}}{mV_g} \end{cases} \quad (26)$$

3.4. Flight state constrains

To enable the UAV to achieve effective rolling and avoid excessive sideslip, the sideslip angle β should be ensured to be sufficiently small as

$$\beta = \psi - \chi \approx 0 \quad (27)$$

On one hand, as shown in Eq.(26), to avoid excessive non-linear disturbances, ϕ needs to be controlled within an appropriate range:

$$\phi_{min} \leq \phi \leq \phi_{max} \quad (28)$$

On the other hand, the lift force is constrained within a specific range, which is manifested as the boundedness of

its load factor, i.e.

$$n_{lf,\min} \leq n_{lf} \leq n_{lf,\max} \quad (29)$$

Furthermore, the symbols d_χ , d_γ respectively represent the external disturbance imposed on the χ and γ -axes, confined within constrained bound L_d as

$$\sqrt{d_\chi^2 + d_\gamma^2} \leq L_d \quad (30)$$

3.5. Look-ahead pursuit guidance law

This section details the approach to the longitudinal and lateral look-ahead pursuit path following guidance law in the presence of constrained disturbance. During the process of the UAV tracking along the current waypoint (x_c, y_c, z_c) , the position errors along the x , y , z -axis directions are defined as

$$e_x = x_c - x_p, \quad e_y = y_c - y_p, \quad e_z = z_c - z_p \quad (31)$$

The longitudinal flight path angle γ_c and the lateral flight path angle χ_c of the Line of Sight (LOS) are defined as

$$\chi_c = \tan^{-1} \frac{y_c - y_p}{x_c - x_p}, \quad \gamma_c = \tan^{-1} \frac{z_c - z_p}{\sqrt{(x_c - x_p)^2 + (y_c - y_p)^2}} \quad (32)$$

The look-ahead pursuit control of UAV considers the problem of following a predetermined path \mathcal{P} as the tracking problem for moving virtual path points. An imaginary target point (x_c, y_c, z_c) traverses along the reference path \mathcal{P} , with LOS vector extending from the UAV to this point, defined as the look-ahead vector L comprised of the lateral component L^{lat} and the longitudinal component L^{lon} , as shown in Figure 4, and the virtual target point $P_c = (x_c, y_c, z_c)$ is defined

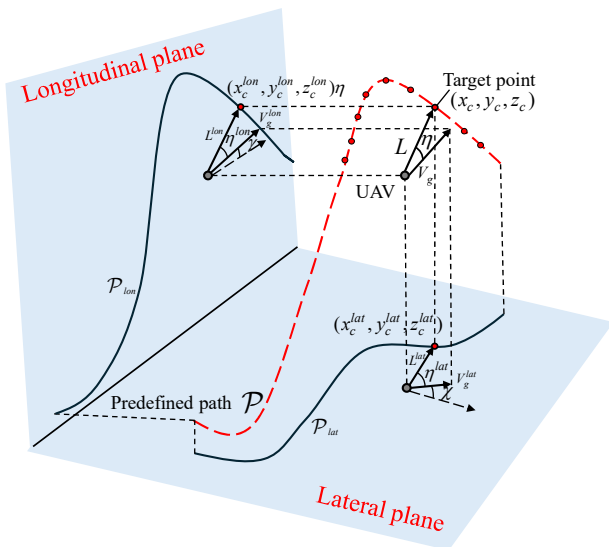


Figure 4: Schematic diagram of look-ahead pursuit guidance law decoupled along the longitudinal and lateral plane projections for a predefined path.

as the nearest point located ahead along the predefined reference path in the direction of velocity as [17]

$$P_c = \underset{(x,y,z) \in \mathcal{P}}{\operatorname{argmin}} |q_L V_g - \sqrt{(x_p - x)^2 + (y_p - y)^2 + (z_p - z)^2}| \quad (33)$$

where q_L represents the coefficient that adaptively adjusts the look-ahead length in relation to the UAV's ground velocity.

During the process of tracking a virtual target point, its first-order derivative $\dot{x}_c, \dot{y}_c, \dot{z}_c$ can be considered as zeros under the condition of not considering abrupt target switching, and its lateral look-ahead angle η^{lat} and longitudinal look-ahead angle η^{lon} can be defined as

$$\eta^{lat} = \chi_c - \chi, \quad \eta^{lon} = \gamma_c - \gamma \quad (34)$$

and η^{lat} is limited to $\eta_{\min}^{lat} \leq \eta^{lat} \leq \eta_{\max}^{lat}$, η^{lon} is limited to $\eta_{\min}^{lon} \leq \eta^{lon} \leq \eta_{\max}^{lon}$.

Specifically, it is precisely because the velocity direction of the UAV can be ensured to be coincide with the LOS, stabilizing the positional errors to zeros in a finite time. This is the foundational principle of look-ahead pursuit control, which will be further elucidated by the following theorem.

Theorem 3. (The fast finite-time stability of look-ahead pursuit guidance law) The e_x , e_y , and e_z will be stabilized to 0 within a finite time

$$T(e_0) \leq \frac{\sqrt{e_x^2(0) + e_y^2(0) + e_z^2(0)}}{V_g \cos \delta^{lon} \cos \delta^{lat}} \quad (35)$$

under

$$\gamma(z_p - z_c) \leq 0 \iff \begin{cases} \eta^{lon} \leq \gamma_c, & z_p \leq z_c \\ \eta^{lon} \geq \gamma_c, & z_p > z_c \end{cases} \quad (36)$$

and there exists $\delta^{lon}, \delta^{lat} < \frac{\pi}{2}$ such that

$$|\eta^{lon}| \leq \delta^{lon}, \quad |\eta^{lat}| \leq \delta^{lat} \quad (37)$$

where initial position error is $e_0 = (e_x(0), e_y(0), e_z(0))^T$.

Proof. There exists

$$\sin \chi = \sin(\chi_c - \eta^{lat}) = \frac{e_y \cos \eta^{lat} - e_x \sin \eta^{lat}}{\sqrt{e_x^2 + e_y^2}} \quad (38)$$

$$\cos \chi = \cos(\chi_c - \eta^{lat}) = \frac{e_y \sin \eta^{lat} + e_x \cos \eta^{lat}}{\sqrt{e_x^2 + e_y^2}} \quad (39)$$

$$\sin \gamma = \sin(\gamma_c - \eta^{lon}) = \frac{e_z \cos \eta^{lon} - \sqrt{e_x^2 + e_y^2} \sin \eta^{lon}}{\sqrt{e_x^2 + e_y^2 + e_z^2}} \quad (40)$$

$$\cos \gamma = \cos(\gamma_c - \eta^{lon}) = \frac{e_z \sin \eta^{lon} + \sqrt{e_x^2 + e_y^2} \cos \eta^{lon}}{\sqrt{e_x^2 + e_y^2 + e_z^2}} \quad (41)$$

and $\dot{x}_p = -\dot{e}_x$, $\dot{y}_p = -\dot{e}_y$, $\dot{z}_p = -\dot{e}_z$. Substitute it into Eq.(21) to obtain the dynamic of e_x, e_y, e_z :

$$\begin{cases} \dot{e}_x = -V_g \frac{e_z \sin \eta^{lon} + \sqrt{e_x^2 + e_y^2} \cos \eta^{lon}}{\sqrt{e_x^2 + e_y^2 + e_z^2}} \frac{e_y \sin \eta^{lat} + e_x \cos \eta^{lat}}{\sqrt{e_x^2 + e_y^2}} \\ \dot{e}_y = -V_g \frac{e_z \sin \eta^{lon} + \sqrt{e_x^2 + e_y^2} \cos \eta^{lon}}{\sqrt{e_x^2 + e_y^2 + e_z^2}} \frac{e_y \cos \eta^{lat} - e_x \sin \eta^{lat}}{\sqrt{e_x^2 + e_y^2}} \\ \dot{e}_z = -V_g \frac{e_z \cos \eta^{lon} - \sqrt{e_x^2 + e_y^2} \sin \eta^{lon}}{\sqrt{e_x^2 + e_y^2 + e_z^2}} \end{cases}$$

we can construct Lyapunov function

$$V(e) = \frac{1}{2}(e_x^2 + e_y^2 + e_z^2) \quad (42)$$

and there exists

$$\begin{aligned} \dot{V}(e) &= \frac{-V_g}{\sqrt{e_x^2 + e_y^2 + e_z^2}} \times [(e_x^2 + e_y^2 + e_z^2) \cos \eta^{lon} \cos \eta^{lat} \\ &\quad + e_z(1 - \cos \eta^{lat})(e_x \cos \eta^{lon} - \sqrt{e_x^2 + e_y^2} \sin \eta^{lon})] \\ &= -V_g [\sqrt{e_x^2 + e_y^2 + e_z^2} \cos \eta^{lon} \cos \eta^{lat} \\ &\quad + e_z(1 - \cos \eta^{lat}) \sin(\gamma_c - \eta^{lon})] \\ &\leq -\sqrt{2} V_g V(e)^{\frac{1}{2}} \cos \delta^{lon} \cos \delta^{lat} \\ &\quad - V_g e_z (1 - \cos \eta^{lat}) \sin(\gamma_c - \eta^{lon}) \end{aligned} \quad (43)$$

Due to the Eq.(36), here $e_z \gamma \geq 0$, i.e.,

$$e_z \sin(\gamma_c - \eta^{lon}) = e_z \sin \gamma \geq 0 \quad (44)$$

Substitute above equation into Eq.(43) that

$$\begin{aligned} \dot{V}(e) &\leq -\sqrt{2} V_g V(e)^{\frac{1}{2}} \cos \delta^{lon} \cos \delta^{lat} \\ &\quad - V_g e_z (1 - \cos \eta^{lat}) \sin(\gamma_c - \eta^{lon}) \\ &\leq -\sqrt{2} V_g V(e)^{\frac{1}{2}} \cos \delta^{lon} \cos \delta^{lat} \end{aligned} \quad (45)$$

Hence, according to the Lemma 2, the e_x, e_y , and e_z will be stabilized to 0 within a finite time, and the settling time is:

$$T(e_0) \leq \frac{\sqrt{2} V(e_0)^{\frac{1}{2}}}{V_g \cos \delta^{lon} \cos \delta^{lat}} = \frac{\sqrt{e_x^2(0) + e_y^2(0) + e_z^2(0)}}{V_g \cos \delta^{lon} \cos \delta^{lat}}$$

The proof is completed. \square

The aforementioned conclusion indicates that look-ahead pursuit guidance law designed for the path angle can guarantee finite-time stabilization of the look-ahead

angle errors, thereby ensuring stabilization of the positional errors.

The objective of this paper is to design the desired control commands ϕ, n_{lf} to ensure that the path following errors can be robustly stabilized within a minimum input energy even when subject to bounded path angle disturbances, which is accomplished through the implementation of improved adaptive longitudinal and lateral look-ahead pursuit control strategy[17].

4. Path Following Controller with Optimal Robustness Indicator

As the core of this study, an optimal path-following controller is designed in this section, with its role in the UAV path-following process illustrated in Figure 5. First, the sufficient conditions for ensuring the robust stability of η^{lon} and η^{lat} are derived. Based on these conditions, a guidance law design method is proposed to minimize the UAV's acceleration energy while guaranteeing the predefined robustness indicator. This method can be formulated as a classic optimization model and efficiently solved within a short time.

4.1. Robustness indicator

We now formally present the specific formulation of the RLLP guidance law. Define the following reference input commands for the autopilot module.

$$\begin{cases} \phi_c = \sin^{-1}(a_{yc}/g) \in [\phi_{\min}, \phi_{\max}] \\ n_{lf,c} = a_{zc}/g \cos \phi_c \in [n_{lf,\min}, n_{lf,\max}] \end{cases} \quad (46)$$

where the acceleration

$$a = (a_{yc}, a_{zc})^T \quad (47)$$

is expressed as

$$\begin{cases} a_{yc} = -V_g f_\chi(\eta^{lat}, \eta^{lon}) \cos \phi / \cos \beta \in [-g, g] \\ a_{zc} = -V_g f_\gamma(\eta^{lat}, \eta^{lon}) + g \cos \gamma \end{cases} \quad (48)$$

Here, f_χ and f_γ determine the specific formulation of the guidance law, with their values directly governing the robustness level of the RLLP guidance law. Building upon the preliminaries, as one of the core theorems of this paper, we characterize the relationships between the functions f_χ, f_γ and the ultimate convergence set of $\eta(t)$, and the convergence rate as follows:

Theorem 4. (Robust stability conditions for η^{lon} and η^{lat}) For the UAV's dynamic model Eq.(25) using the guidance law Eq.(46) and Eq.(48), let

$$f(\eta) = \begin{pmatrix} f_\chi(\eta^{lat}, \eta^{lon}) \\ f_\gamma(\eta^{lat}, \eta^{lon}) \end{pmatrix}, \quad \eta = \begin{pmatrix} \eta^{lat} \\ \eta^{lon} \end{pmatrix} \quad (49)$$

where $f(0) = (0, 0)^T$, the perturbation term is

$$d = (d_\chi, d_\gamma)^T, \quad \|d\|_2 \leq L_d \quad (50)$$

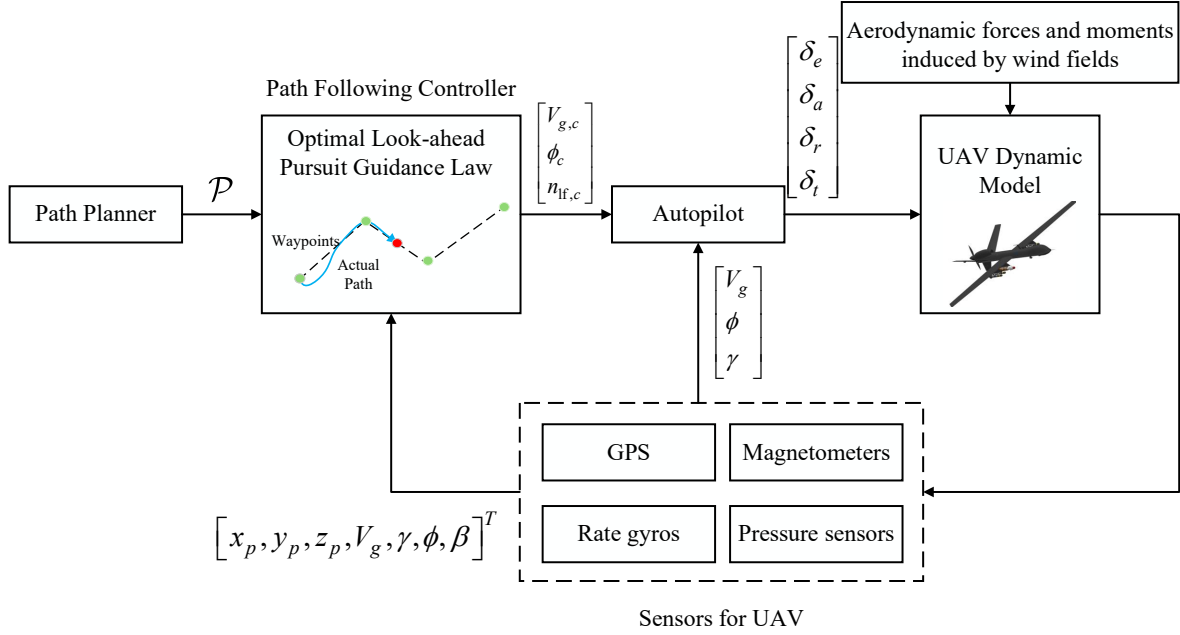


Figure 5: Schematic diagram of path following control via optimal look-ahead pursuit guidance law.

If f is L_c -co-Lipschitz on the neighbor of origin,

$$\left\| \frac{\partial f(0)}{\partial \eta} \right\|_2 \leq L_f \quad (51)$$

and

$$R(f) = -\lambda_{\max} \left(\left[\frac{\partial f(0)}{\partial \eta} \right]^T + \frac{\partial f(0)}{\partial \eta} \right) > 0 \quad (52)$$

Then the ultimate trajectory of the state $\eta(t)$, for any initial value $\eta(0)$, $\eta(t)$ will exponentially converge to the following global random attractor $S(0)$ at least the rate of $R(f)$ as $t \rightarrow \infty$:

$$\eta(t) \rightarrow S(0) = \{ \eta : \|\eta\|_2 \leq 2L_d I(f) \} \quad (53)$$

where

$$I(f) = \frac{L_f}{L_c} \frac{1}{R(f)} \quad (54)$$

Proof. By substituting Eq.(46) and Eq.(48) into Eq.(25), the following result can be derived:

$$\begin{cases} \dot{\chi} = -f_{\chi}(\eta^{lat}, \eta^{lon}) + d_{\chi} \\ \dot{\gamma} = -f_{\gamma}(\eta^{lat}, \eta^{lon}) + d_{\gamma} \end{cases} \quad (55)$$

When tracking waypoints within each flight segment, since the every waypoint being tracked is fixed, i.e., $\dot{\gamma}_c = \dot{\chi}_c = 0$, which is equivalent to $\dot{\chi} = -\dot{\eta}_{lat}$, $\dot{\gamma} = -\dot{\eta}_{lon}$. Substituting it into the above equation yields:

$$\begin{cases} \dot{\eta}^{lat} = f_{\chi}(\eta^{lat}, \eta^{lon}) - d_{\chi} \\ \dot{\eta}^{lon} = f_{\gamma}(\eta^{lat}, \eta^{lon}) - d_{\gamma} \end{cases} \quad (56)$$

By Theorem 2 and Remark 3, the conclusion follows, hence the proof is completed. \square

Remark 4. If there exists the robust stability constraint for the predefined lowerbound value $R^* > 0$ that $R(f) \geq R^*$, at this point, the exponential convergence rate is at least R^* , and the $\eta(t) = (\eta^{lat}(t), \eta^{lon}(t))^T$ of the final trajectory is converged to the interior of the following region:

$$\sqrt{\eta^{lat}(t)^2 + \eta^{lon}(t)^2} \leq \frac{2L_d L_f}{R^* L_c}, \quad t \rightarrow \infty \quad (57)$$

here f is L_c -co-Lipschitz over

$$X = \left\{ (\eta^{lat}, \eta^{lon}) : |\eta^{lat}| < \frac{\pi}{2}, |\eta^{lon}| < \frac{\pi}{2} \right\} \quad (58)$$

We will introduce several classic forms of $f(\eta)$, and based on these, analyze their $R(f)$ and $I(f)$ as tabulated in Table 1.

4.2. The optimization model for $I(f)$

According to Theorem 3, we can minimize the finite convergence time $T(e_0)$ by reducing the absolute upper bounds δ^{lon} and δ^{lat} of η^{lon} and η^{lat} as much as possible, which can be achieved by minimizing the attractor size $I(f)$. In this section, an optimal $f = (f_{\chi}, f_{\gamma})^T$ is selected to minimize the attractor size $I(f)$ under constrained acceleration limits and exponential convergence rate lowerbound, expressed as

$$\begin{aligned} & \min_f I(f) \\ & \text{s.t.} \begin{cases} R(f) \geq R^* \\ a_{\min} \leq a \leq a_{\max} \end{cases} \end{aligned} \quad (59)$$

The optimization model is formulated to minimize the attractor size subject to two constraints: acceleration magnitude limits and a minimum exponential convergence rate to the attractor (predefined as $R^* > 0$).

Table 1

 The L_f , L_c , $R(f)$, $I(f)$ for some classic types of f .

Type	$f_\chi(\eta^{lat}, \eta^{lon})$	$f_\gamma(\eta^{lat}, \eta^{lon})$	L_f	L_c	$R(f)$	$I(f)$
x	$-k_\chi \eta^{lat}, k_\chi > 0$	$-k_\gamma \eta^{lon}, k_\gamma > 0$	$\max\{k_\chi, k_\gamma\}$	$\min\{k_\chi, k_\gamma\}$	$2 \min\{k_\chi, k_\gamma\}$	$\max\{k_\chi, k_\gamma\}/2 \min\{k_\chi, k_\gamma\}^2$
$\tan(x)$	$-k_\chi \tan \eta^{lat}, k_\chi > 0$	$-k_\gamma \tan \eta^{lon}, k_\gamma > 0$	$\max\{k_\chi, k_\gamma\}$	$\min\{k_\chi, k_\gamma\}$	$2 \min\{k_\chi, k_\gamma\}$	$\max\{k_\chi, k_\gamma\}/2 \min\{k_\chi, k_\gamma\}^2$
$\exp(x)$	$1 - e^{k_\chi \eta^{lat}}, k_\chi > 0$	$1 - e^{k_\gamma \eta^{lon}}, k_\gamma > 0$	$\max\{k_\chi, k_\gamma\}$	$\min\{k_\chi e^{-\frac{\pi}{2} k_\chi}, k_\gamma e^{-\frac{\pi}{2} k_\gamma}\}$	$2 \min\{k_\chi, k_\gamma\}$	$\max\{k_\chi, k_\gamma\}/2 \min\{k_\chi, k_\gamma\} L_c$
$\sin(x)$	$-k_\chi \sin \eta^{lat}, k_\chi > 0$	$-k_\gamma \sin \eta^{lon}, k_\gamma > 0$	$\max\{k_\chi, k_\gamma\}$	$2 \min\{k_\chi, k_\gamma\}/\pi$	$2 \min\{k_\chi, k_\gamma\}$	$\pi \max\{k_\chi, k_\gamma\}/4 \min\{k_\chi, k_\gamma\}^2$
linear	$k_\chi^{lat} \eta^{lat} + k_\chi^{lon} \eta^{lon}$	$k_\gamma^{lat} \eta^{lat} + k_\gamma^{lon} \eta^{lon}$	$\ K\ _2$	$\ K^{-1}\ _2^{-1}$	$-\lambda_{\max}(K^T + K) > 0$	$-\ K\ _2 \ K^{-1}\ _2^{-1} / \lambda_{\max}(K^T + K)$

To simplify the presentation, we use a linear model to characterize the form of $f(\eta)$, i.e.,

$$f(\eta) = K\eta = Fk \quad (60)$$

where

$$K = \begin{pmatrix} k_\chi^{lat} & k_\chi^{lon} \\ k_\gamma^{lat} & k_\gamma^{lon} \end{pmatrix}, \eta = \begin{pmatrix} \eta^{lat} \\ \eta^{lon} \end{pmatrix} \quad (61)$$

$$F = \begin{pmatrix} \eta^{lat} & 0 & \eta^{lon} & 0 \\ 0 & \eta^{lat} & 0 & \eta^{lon} \end{pmatrix} \quad (62)$$

$$k = \text{vec}(K) = (k_\chi^{lat}, k_\gamma^{lat}, k_\chi^{lon}, k_\gamma^{lon})^T \quad (63)$$

The acceleration a can be described as:

$$a = b + \Lambda f(\eta) = b + \Lambda Fk \quad (64)$$

where

$$b = \begin{pmatrix} 0 \\ g \cos \gamma \end{pmatrix}, \Lambda = \begin{pmatrix} -V_g \frac{\cos \phi}{\cos \beta} & \\ & -V_g \end{pmatrix} \quad (65)$$

Furthermore, we can estimate the L_f of $f(\eta)$ at the origin by its Jacobian:

$$L_f = \left\| \frac{\partial f(0)}{\partial \eta} \right\|_2 = \|K\|_2 \quad (66)$$

Under the invertibility of K , the co-Lipschitz coefficient L_c of $f(\eta)$ can be estimated by

$$L_c = \frac{1}{\|K^{-1}\|_2} \quad (67)$$

which is derived from the following process, $\forall \eta_1, \eta_2$,

$$\begin{aligned} \|\eta_1 - \eta_2\|_2 &= \|K^{-1}(K\eta_1 - K\eta_2)\|_2 \\ &\leq \|K^{-1}\|_2 \|K\eta_1 - K\eta_2\|_2 \end{aligned} \quad (68)$$

i.e.,

$$\|f(\eta_1) - f(\eta_2)\| \geq \frac{\|\eta_1 - \eta_2\|_2}{\|K^{-1}\|_2} \quad (69)$$

Here, the exponential convergence rate $R(f) = R(k)$ can be characterized by:

$$\begin{aligned} R(k) &= -\lambda_{\max}(K^T + K) \\ &= -\lambda_{\max} \begin{pmatrix} 2k_\chi^{lat} & k_\chi^{lon} + k_\gamma^{lat} \\ k_\chi^{lon} + k_\gamma^{lat} & 2k_\gamma^{lon} \end{pmatrix} \\ &= -\left(k_\chi^{lat} + k_\gamma^{lon} + \sqrt{(k_\chi^{lat} - k_\gamma^{lon})^2 + (k_\chi^{lon} + k_\gamma^{lat})^2} \right) \end{aligned} \quad (70)$$

To summarize, the final optimization model is transformed into a nonlinear model for parameter k -optimization as follows

$$\begin{aligned} \min_k I(k) &= -\frac{\|K\|_2 \|K^{-1}\|_2}{\lambda_{\max}(K^T + K)} \\ \text{s.t.} \quad &\begin{cases} R(k) \geq R^* > 0 \\ a_{\min} - b \leq \Lambda Fk \leq a_{\max} - b \end{cases} \end{aligned} \quad (71)$$

The pseudocode of the path following controller with optimal robustness indicator algorithm is as Alg.1. As the core of

Algorithm 1 The look-ahead pursuit guidance law with optimal robustness indicator

Input: The reference waypoints set \mathcal{P} , current UAV's state measured by $(x_p, y_p, z_p, V_g, \gamma, \phi, \beta)$, predefined robustness indicator R^*

Output: The optimal guidance law $\phi_c^*, n_{lf,c}^*$

- 1: Calculate the virtual target point P_c by Eq.(33).
- 2: Calculate the reference angles χ_c, γ_c by Eq.(32).
- 3: Calculate the look-ahead angles η^{lon}, η^{lat} by Eq.(34).
- 4: **if** the current waypoint P_c tracked by the UAV undergoes a change **then**
- 5: Solve the optimization model Eq.(71) to obtain the optimal coefficient k^* .
- 6: **else**
- 7: Keep k^* unchanged.
- 8: **end if**
- 9: Calculate optimal acceleration a^* from k^* by Eq.(48) and Eq.(60).
- 10: Obtain the $\phi_c^*, n_{lf,c}^*$ by Eq.(46).

the algorithm, lines 4-8, the optimization model is resolved upon each switch of reference waypoints. Namely, a fixed optimal coefficient k^* is employed to derive the optimal guidance law for path following during tracking of each waypoint, whereas re-optimization is necessitated to solve for the optimal k^* during waypoint transitions.

5. The Autopilot

In aerospace applications, autopilot serves as the primary guidance systems for UAVs. Specifically, the autopilot maintains full flight envelope control across all operational

phases, including takeoff, waypoint navigation, and landing. The primary function of the autopilot is to accurately track the reference commands ϕ_c , $n_{lf,c}$ and $V_{g,c}$ calculated by the path following controller. In this section, suitable controller designs for roll angle, load factor, and groundspeed will be presented, which are based on Proportional-Integral (PI) control algorithms tailored to the available sensors and computational resources.

5.1. Roll angle controller

For the roll angle controller, the feedback is generated by computing the error between the commanded roll angle ϕ_c and the actual roll angle ϕ measured by rate gyros. A PI controller is used to calculate the aileron deflection command δ_a as

$$\delta_a = k_p^\phi(\phi_c - \phi) + k_i^\phi \int (\phi_c - \phi) dt - k_d^\phi p \quad (72)$$

where k_p^ϕ and k_i^ϕ are the corresponding PI controller coefficients, p is the roll angle rate measured by rate gyros, and k_d^ϕ is its corresponding coefficient. The purpose of adding the compensation term for p is to ensure the low-inertia requirement when tracking ϕ_c . The integral anti-windup mechanism prevents integral term saturation due to prolonged error accumulation, while amplitude limiting is applied to δ_a to ensure it stays within the actuator's operational range of $[-\pi/4, \pi/4]$. The overall control system

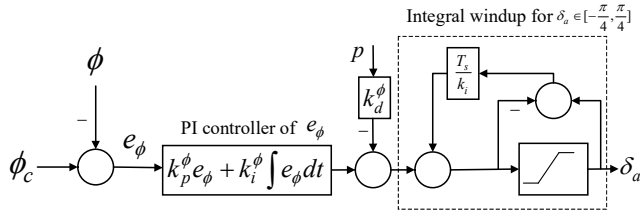


Figure 6: Roll angle control is achieved using a PI controller with integral windup limitation.

block diagram is shown in Figure.6.

5.2. Load factor controller

Similarly, the load factor controller also utilizes the feedback error between the reference load factor $n_{lf,c}$ and the measured load factor n_{lf} , where n_{lf} can be estimated by the following equation:

$$n_{lf} = \frac{V_g \dot{\gamma}}{g \cos \phi} + \frac{\cos \gamma}{\cos \phi} \quad (73)$$

where the flight-path angle γ of the UAV and its derivative $\dot{\gamma}$ are measured by GPS and magnetometers, while the roll angle ϕ is obtained by integrating the value measured by rate gyros. For the tracking control of $n_{lf,c}$, successive loop closure (SLC) PI controllers are implemented. Specifically, the outer loop employs a PI controller with anti-windup to regulate the reference pitch angle θ_c as follows

$$\hat{\theta}_c = k_p^\theta(n_{lf,c} - n_{lf}) + k_i^\theta \int (n_{lf,c} - n_{lf}) dt \quad (74)$$

$$\theta_c = \text{Integral-windup}(\hat{\theta}_c), \theta_c \in [-\frac{\pi}{6}, \frac{\pi}{6}] \quad (75)$$

This design leverages the monotonically increasing relationship between the pitch angle and UAV lift force within a defined operational range, enabling precise tracking of $n_{lf,c}$ via θ_c control. Concurrently, mirroring the roll angle control architecture, the inner-loop pitch angle controller adopts an identical anti-windup PI control scheme for the elevator δ_e as follows

$$\hat{\delta}_e = k_p^\theta(\theta_c - \theta) + k_i^\theta \int (\theta_c - \theta) dt - k_d^\theta q \quad (76)$$

$$\delta_e = \text{Integral-windup}(\hat{\delta}_e), \delta_e \in [-\frac{\pi}{4}, \frac{\pi}{4}] \quad (77)$$

where k_p^θ and k_i^θ are the corresponding PI controller coefficients, q is the pitch angle rate measured by rate gyros, and k_d^θ is its corresponding coefficient. The SLC control system configuration is depicted in Figure 7.

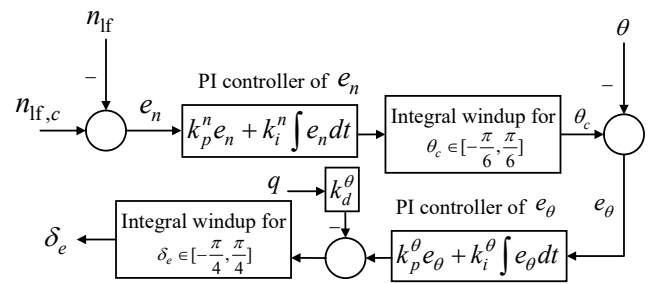


Figure 7: Load factor control is achieved using successive loop closure (SLC) PI controllers with integral windup limitation.

5.3. Groundspeed controller

For the groundspeed controller, under the constraint of small pitch angles, constant groundspeed control is realized by directly regulating the throttle opening δ_r . As shown in Figure 8, the control scheme integrates a PI controller with anti-windup, where the velocity error $e_V = V_{g,c} - V_g$ is processed through low-pass filtered differentiation. This

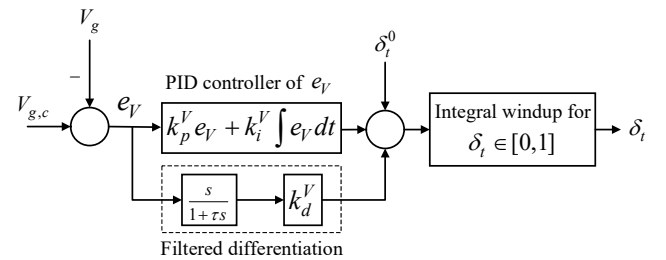


Figure 8: Groundspeed control is achieved using a PI controller with filtered differentiation and integral windup limitation.

filtering mechanism serves dual objectives: (1) suppressing high-frequency noise to eliminate controller oscillations triggered by measurement noise, and (2) alleviating abrupt

Table 2

Definition of some parameters.

Param	Value	Implication	Param	Value	Implication
g	9.81m/s ²	Gravitational coefficient	τ	5s	Time coefficient for groundspeed controller
$x_p(0)$	0 m	UAV's x_p along the north at initial time	k_χ	0.5	Hyperparameter for f in the RLLP
$y_p(0)$	0 m	UAV's y_p along the east at initial time	k_γ	0.5	Hyperparameter for f in the RLLP
$z_p(0)$	40 m	UAV's z_p along the height at initial time	δ_t^0	0.06	Initial throttle openings
$\phi(0)$	0 deg	UAV's roll angle at initial time	k_p^V	7.06	Proportional gain for groundspeed controller
$\theta(0)$	4.09 deg	UAV's pitch angle at initial time	k_i^V	0.88	Integral gain for groundspeed controller
$\psi(0)$	0 deg	UAV's yaw angle at initial time	k_d^V	0	Derivative gain for groundspeed controller
$\gamma(0)$	0 deg	UAV's flight-path angle at initial time	k_p^ϕ	2.14	Proportional gain for roll angle controller
$\chi(0)$	0 deg	UAV's course angle at initial time	k_i^ϕ	0.10	Integral gain for roll angle controller
q_L	0.25	Adaptive coefficient for look-ahead length	k_d^ϕ	1.23	Derivative gain for roll angle controller
$V_{g,c}$	13m/s	Reference groundspeed	k_p^a	1.50	Proportional gain for load factor controller
ϕ_{\min}	-45°	The minimum value of roll angle	k_i^a	0.50	Integral gain for load factor controller
ϕ_{\max}	45°	The maximum value of roll angle	k_p^θ	0.55	Proportional gain for pitch angle controller
$n_{lf,\min}$	0	The minimum value of load factor	k_i^θ	0	Integral gain for pitch angle controller
$n_{lf,\max}$	2.1	The maximum value of load factor	k_d^θ	0.14	Derivative gain for pitch angle controller
$a_{yc,\min}$	-9.81m/s ²	The minimum value of a_{yc}	$a_{yc,\max}$	9.81m/s ²	The maximum value of a_{yc}

derivative-term surges caused by setpoint transients. The control algorithm is described as follows:

$$\begin{aligned} \hat{\delta}_t &= \delta_t^0 + k_p^V(V_{g,c} - V_g) + k_i^V \int (V_{g,c} - V_g) dt \\ &\quad + k_d^V \frac{\dot{V}_{g,c} - \dot{V}_g}{1 + \tau s} \end{aligned} \quad (78)$$

$$\delta_t = \text{Integral-windup}(\hat{\delta}_t), \delta_t \in [0, 1] \quad (79)$$

where k_p^V , k_i^V , k_d^V are the corresponding controller coefficients, and τ is its time coefficient, δ_t^0 is the initial throttle openin.

6. Simulation

In this section, we first validate the proposed robustness indicator theory in a complex urban terrain environment. Second, a comprehensive experimental validation is performed on the path-following performance of the Robust Longitudinal and Lateral Look-ahead Pursuit (RLLP) guidance law. Additionally, by comparing RLLP with its optimal robustness indicator counterpart (Optimal-RLLP), we demonstrate significant enhancements in multiple critical performance metrics, thus verifying the rationality and superiority of Optimal-RLLP. Finally, the path-following performance across different key parameters is systematically investigated. The experimental environment is configured as a low-altitude path-following experiment in a dense urbanization environment with 36 high-rise buildings. The waypoints of the path, designed to mimic real-world urban navigation tasks, are shown in Figure 10, featuring sharp turns and altitude changes. Meanwhile, the key hyperparameter configurations in this experiment, including lookahead distance, control gain, and UAV's initial state, etc., are presented in Table 2, which are carefully tuned based on prior robustness analysis. The UAV model required for



Figure 9: The physical demonstration of Aerosonde aircraft.

simulations is considered as a type of small and Miniature Air Vehicle (MAV), referred to as Aerosonde, specifically a fixed-wing configuration with a 1.2m wingspan, and its physical and aerodynamic parameters specified below are reported in Ref.[26]. The Aerosonde is powered by a small four-stroke engine. Originally designed for scientific missions, the Aerosonde gained notoriety in 1998 as the first UAV to cross the Atlantic Ocean. Denoted by the acronym MAV, its six-degree-of-freedom dynamic model, aerodynamic coefficient tables, autopilot control architecture, and extended Kalman filter-based state estimation are all derived from the benchmark Ref.[27], ensuring the simulation fidelity in urban low-altitude scenarios.

6.1. Validation of the theoretical framework

To validate the correctness of the proposed theory involving $I(f)$, including Theorem 3, Theorem 4, and Remark 4, we conducted comparative experiments on the RLLP guidance law with four distinct function forms f (including the x , $\tan(x)$, $\exp(x)$, $\sin(x)$, as listed in Table 1). The experiments were executed under $k_\chi = 0.5$ and $k_\gamma = 0.5$, and

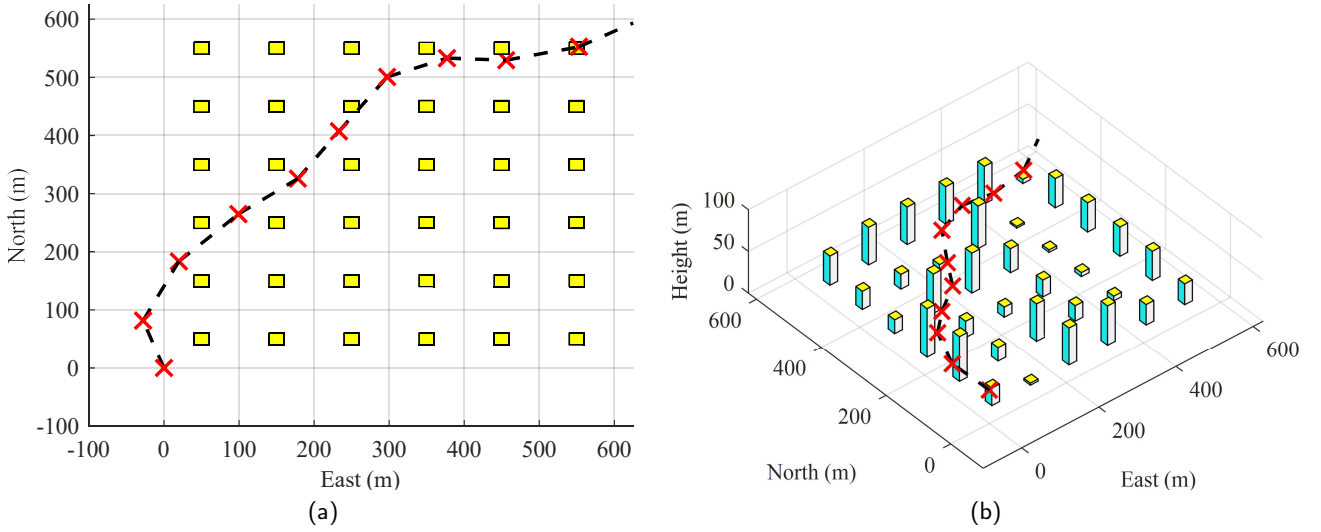


Figure 10: Top view and side view of a sophisticated non-smooth low-altitude urban path used for path-following experiments, where the red crosses symbolize waypoints. (a): Top view; (b): Side view.

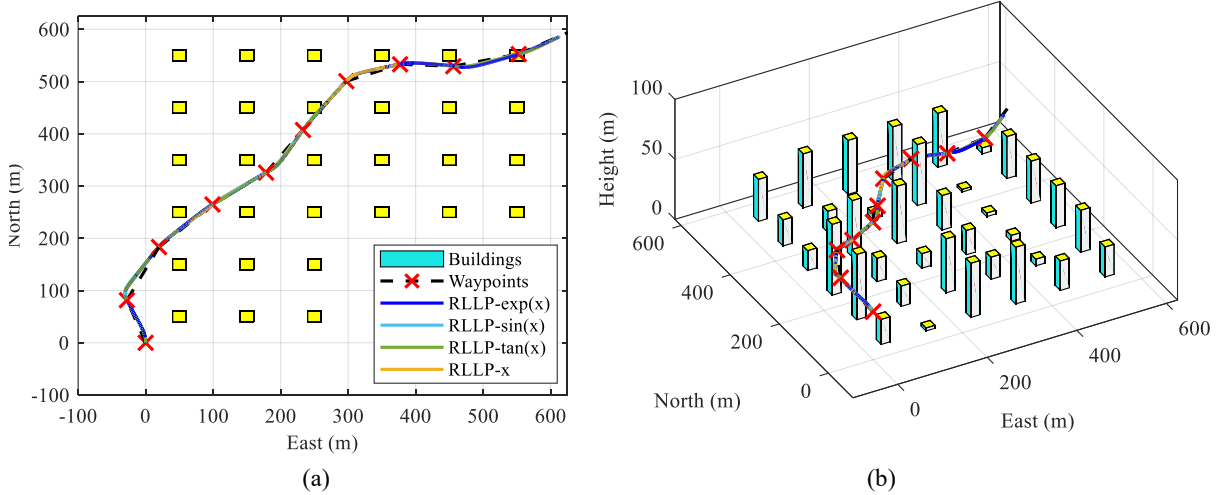


Figure 11: Simulation comparison of UAV tracking trajectory for reference waypoints based on different f . (a): Top view; (b): Side view.

the corresponding path-following trajectories are visualized in Figure 11.

As demonstrated in Figure 11, all RLLP guidance laws corresponding to different f achieve precise waypoint tracking with near-straight trajectories in each segment. To quantify the performance discrepancies, we analyze two key metrics during path following:

$$\|\eta\|_2 = \sqrt{(\eta^{lon})^2 + (\eta^{lat})^2} \quad (80)$$

$$d = \sqrt{(x_c - x_p)^2 + (y_c - y_p)^2 + (z_c - z_p)^2} \quad (81)$$

as presented in Figure 12. First, subplot (a) shows that for any f , $\|\eta\|_2$ converges to a minimal neighborhood (not necessarily zero) in each segment. The final convergence invariant sets of all f nearly coincide, except for RLLP-exp(x), which exhibits a slightly higher invariant set—this is attributed to its higher $I(f)$, validating Theorem 4. Second, subplot (b)

reveals that despite $\|\eta\|_2$ not converging to the origin, d for all RLLP variants converges to zero within finite time with linear convergence profiles. The convergence slopes across segments are consistent, corresponding to a UAV groundspeed of 13 m/s, confirming the validity of Theorem 3. Finally, to quantitatively evaluate the trackability of the autopilot to the proposed RLLP guidance law commands with different f , we analyzed the tracking errors of V_g , ϕ , and n_{lf} against their reference values $V_{g,c}$, ϕ_c , $n_{lf,c}$ during path following, as depicted in Figure 13. The results show that across all trajectory segments and waypoint tracking tasks, RLLP guidance laws with different f consistently ensure rapid stabilization of tracking errors, demonstrating the autopilot's robust control performance for the proposed RLLP framework.

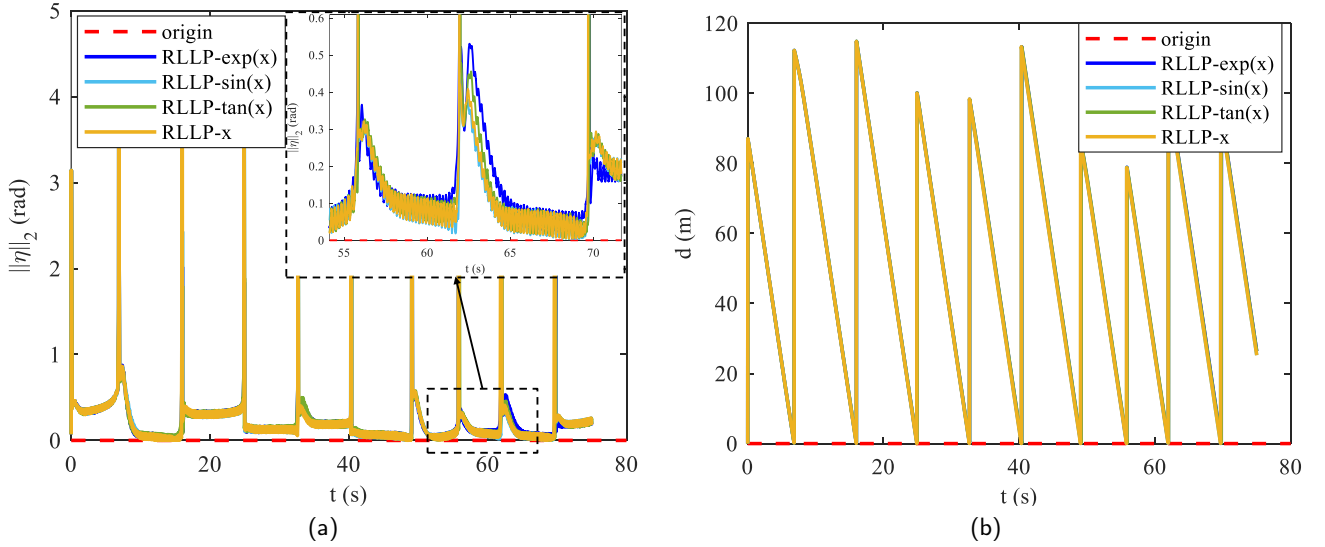


Figure 12: Comparison experiments of four algorithms including RLLP-exp(x), RLLP-sin(x), RLLP-tan(x), RLLP- x on convergence indicators $\|\eta\|_2$ and d . (a) Comparison experiment on $\|\eta\|_2$; (b) Comparison experiment on d .

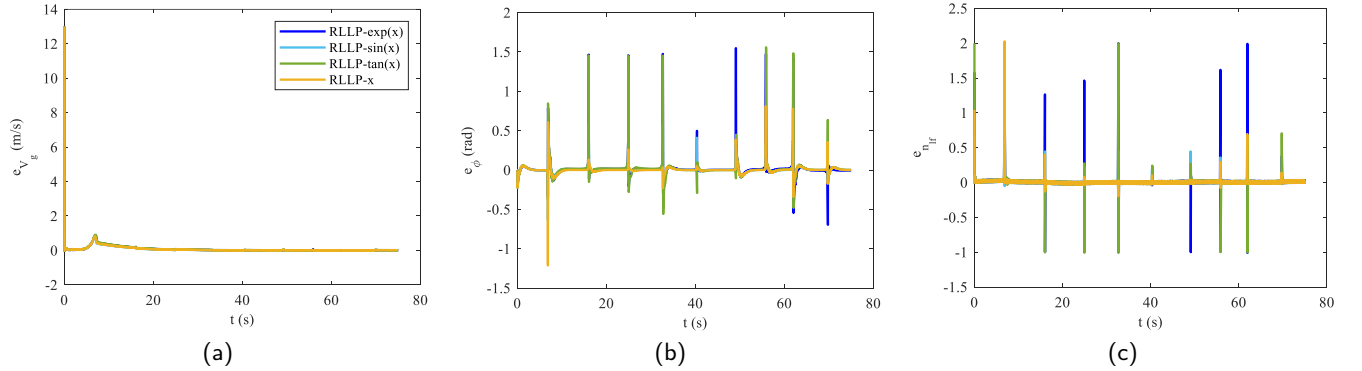


Figure 13: The tracking error curves of the autopilot for the reference signals $V_{g,c}$, ϕ_c , and $n_{ff,c}$. (a): Tracking error for $V_{g,c}$; (b): Tracking error for ϕ_c ; (c): Tracking error for $n_{ff,c}$.

6.2. Path-following experiment of RLLP

In this section, we will study the path-following performance of the Optimal-RLLP guidance law and conduct a comparative analysis with classical algorithms.

6.2.1. The performance of Optimal-RLLP

Figure 14 demonstrates the path-following process of the Optimal-RLLP guidance law, presenting the UAV's actual trajectory and attitude. As clearly shown in the figure, the actual trajectory closely adheres to the straight-line segments of reference waypoints with high precision during path following. The autopilot effectively tracks the guidance law's reference commands $V_{g,c}$, ϕ_c , and $n_{ff,c}$. Since the optimization objective prioritizes minimizing $I(f)$, the reference commands tend to exhibit pronounced oscillations, a characteristic indicating that Optimal-RLLP possesses superior sensitivity. The time-series curves of η^{lat} , η^{lon} , and $\|\eta\|_2$ for the Optimal-RLLP guidance law are depicted in Figure 16. Notably, both η^{lat} and η^{lon} stabilize within a minimal range around the origin in the lateral and longitudinal planes, with

their fluctuation amplitudes consistently constrained below 0.4rad. Under optimal conditions, $\|\eta\|_2$ can even exhibit stable fluctuations within a narrow band of less than 0.05rad. This behavior effectively ensures that the UAV's actual trajectory achieves precise tracking of reference waypoints across the north, east, and height dimensions. As shown in Figure 17, the tracking error for each waypoint is maintained below 1m.

6.2.2. Comparison for RLLP and classical methods

To further demonstrate the superiority of the Optimal-RLLP guidance law, comparative analyses were conducted against the virtual vector field method with Dubins curve connections (VF-Dubins[27]), the virtual vector field method with straight-line connections (VF-Line[15]), and the RLLP guidance law with the functional form $f = \sin(x)$ (RLLP-sin(x)). The UAV tracking trajectories for reference waypoints under the four guidance laws are illustrated in Figure 18. Notably, Optimal-RLLP outperforms the other three methods in straight-line path tracking, a feature indicative of

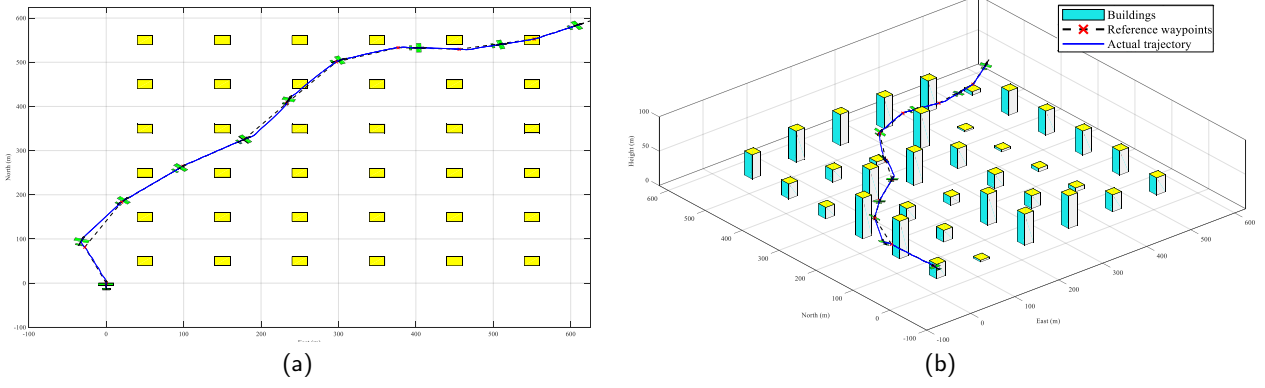


Figure 14: Simulation of UAV tracking trajectory for reference waypoints based on Optimal RLLP. (a): Top view; (b): Side view.

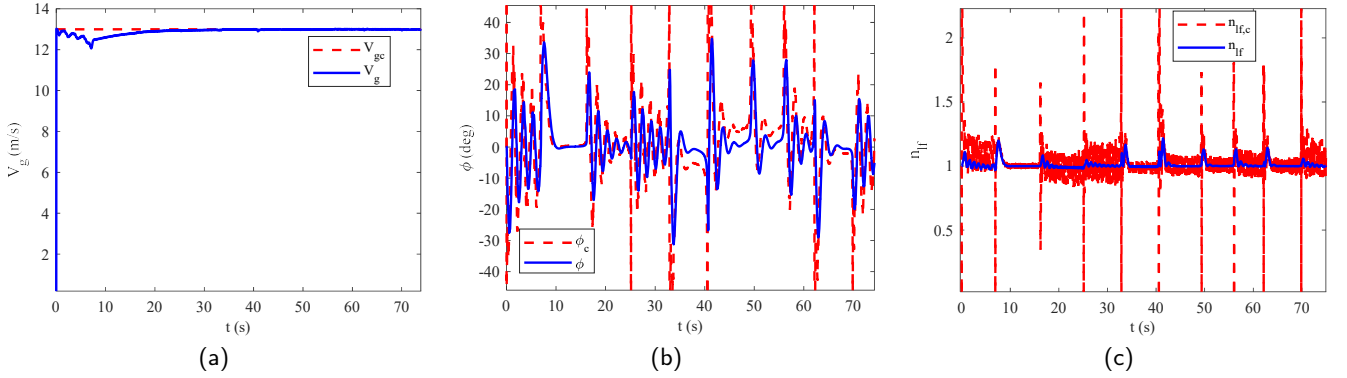


Figure 15: The tracking curves of the autopilot for the reference signals $V_{g,c}$, ϕ_c , and $n_{f,c}$. (a): Tracking curve of $V_{g,c}$; (b): Tracking curve of ϕ_c ; (c): Tracking curve of $n_{f,c}$.

its superior disturbance rejection capability. This advantage is further manifested in smoother waypoint transitions, where the UAV executes turns with smaller curvatures when switching between adjacent waypoints. The superiority of Optimal-RLLP is attributed to the characteristics visualized in Figure 19. In the time-series curve of $\|\eta\|_2$, only Optimal-RLLP and RLLP-sin(x) guidance law efficiently stabilize $\|\eta\|_2$ within each trajectory segment, while VF-Dubins and VF-Line methods exhibit significant oscillations. Compared

with RLLP-sin(x), Optimal-RLLP demonstrates a higher exponential convergence rate, enabling faster stabilization to a smaller steady-state range under more complex disturbances. This feature is precisely what endows Optimal-RLLP with enhanced robustness.

6.3. Robustness under atmospheric disturbances

This section discusses wind-induced atmospheric disturbances and their influence on aircraft dynamics, followed by an analysis of RLLP-sin(x) robustness under varying

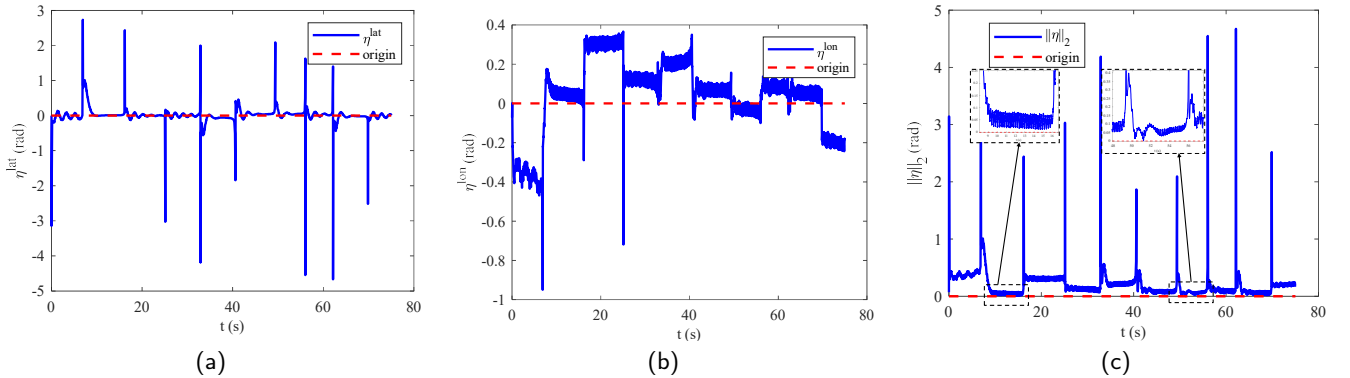


Figure 16: Time-series curves of η^{lat} , η^{lon} , and $\|\eta\|_2$ during path-following process. Notably, $\|\eta\|_2$ converges nearly to the origin in each tracking instance. (a): Time-series curve of η^{lat} ; (b): Time-series curve of η^{lon} ; (c): Time-series curve of $\|\eta\|_2$.

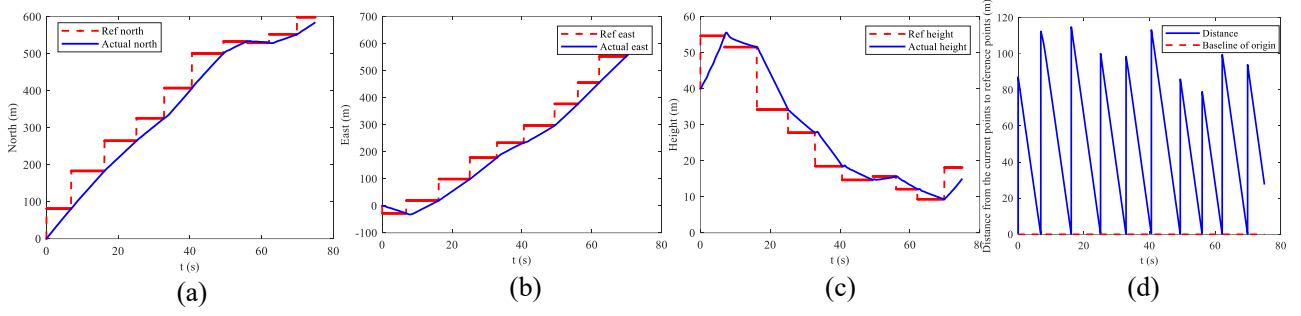


Figure 17: Time-series curves of x_p , y_p , z_p and the relative distance $d = \sqrt{(x_c - x_p)^2 + (y_c - y_p)^2 + (z_c - z_p)^2}$ during path-following process when UAV follows the reference waypoints. Notably, d converges nearly to the origin in each tracking instance. (a): Time-series curve of x_p ; (b): Time-series East curve of y_p ; (c): Time-series curve of z_p ; (d): Time-series curve of d .

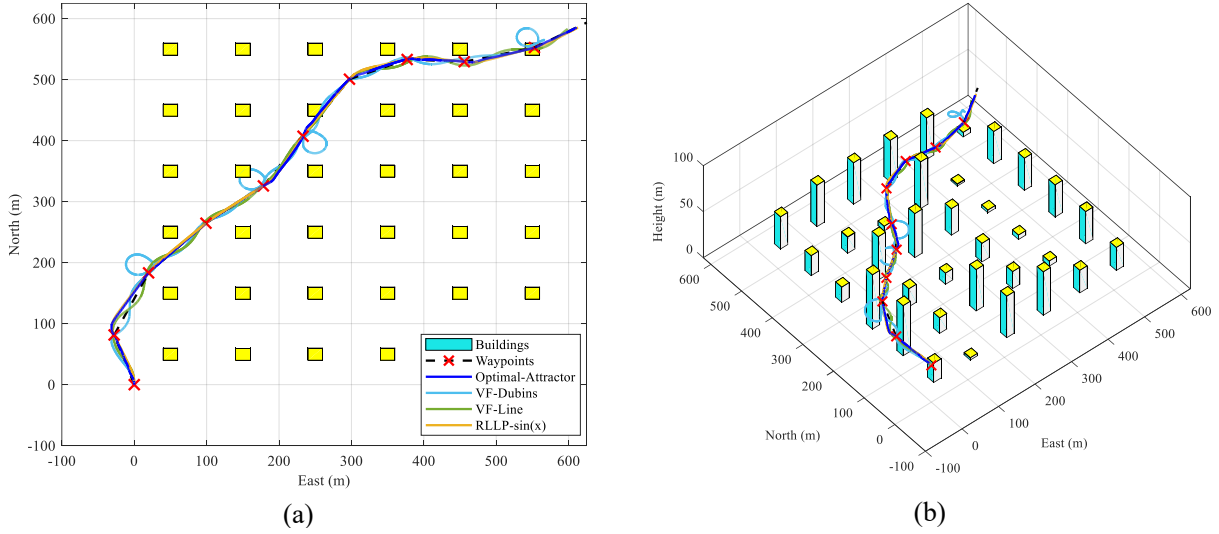


Figure 18: Simulation comparison of UAV tracking trajectory for reference waypoints based on Optimal RLLP, VF-Dubins, VF-line, RLLP-sin(x). (a): Top view; (b): Side view.

disturbance intensities and algorithm parameters. Wind and atmospheric disturbances affect the airspeed V_a , angle-of-attack α , and sideslip angle β . These parameters mediate the impact of wind on aerodynamic forces and moments, thereby influencing aircraft motion. The airspeed V_a is defined as the velocity of the airframe relative to the surrounding air mass, while the wind velocity V_w denotes the velocity of the air mass relative to the ground. For simulation purposes, the total wind vector is decomposed as $V_w = V_{w_s} + V_{w_g}$, where V_{w_s} is a constant vector representing steady ambient wind, and V_{w_g} is a stochastic process modeling wind gusts and other atmospheric disturbances. The ambient wind is typically expressed in the inertial frame as $V_{w_s} = (w_{n_s}, w_{e_s}, w_{d_s})^T$, with w_{n_s} , w_{e_s} , and w_{d_s} denoting steady wind speeds in the north, east, and down directions, respectively. The stochastic gust component is described in the aircraft body frame as $V_{w_g} = (u_{w_g}, v_{w_g}, w_{w_g})^T$. Here, the non-steady gust portion is modeled using white noise filtered through a linear time-invariant system based on the von Kármán turbulence spectrum [28] within the Dryden

Table 3

Some different types of disturbances caused by wind field where U is the uniformly distributed random numbers over the interval $[0,1]$.

Types	V_{w_s} (m/s)	V_{w_g} (m/s)
w_1	(5,0,0)	(0,0,0)
w_2	(5,5,0)	(0,0,0)
w_3	(5,5,2)	(0,0,0)
w_4	(10,10,2)	(0,0,0)
w_5	(5,5,2)	$(-0.25+0.5U, -0.125+0.25U, -0.125+0.25U)$
w_6	(5,5,2)	$(-0.5+U, -0.25+0.5U, -0.25+0.5U)$

transfer functions [27]. The Dryden gust model parameters specified in MIL-F-8785C [29] are: turbulence intensities along body-frame axes $\sigma_u = \sigma_v = 2.12$ m/s, $\sigma_w = 1.4$ m/s; spatial wavelengths $L_u = L_v = 200$ m, $L_w = 50$ m. The influence mechanisms of specific aerodynamic forces and moments are detailed in Ref.[27]. To investigate the path-following performance of RLLP-type algorithms under

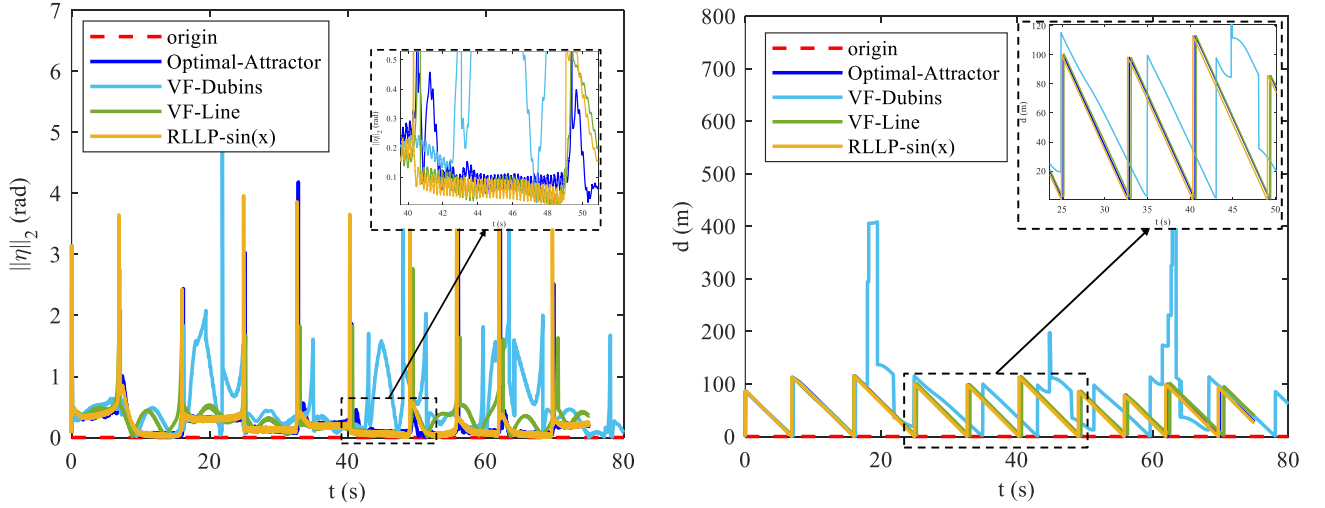


Figure 19: Comparison experiments of four algorithms including Optimal RLLP, VF-Dubins, VF-Line, and RLLP-sin(x) on convergence indicators $\|\eta\|_2$ and d . (a) Comparison experiment on $\|\eta\|_2$; (b) Comparison experiment on d .

Table 4

Some different types of k_x and k_y for the RLLP-sin(x).

Types	(k_x, k_y)	$I(f)$	$R(f)$
k_1	(0.5,0.5)	0.5π	1
k_2	(0.5,1)	π	1
k_3	(1,0.5)	π	1
k_4	(1,1)	0.25π	2
k_5	(2,2)	0.125π	4
k_6	(4,4)	0.0625π	8
k_7	(0.25,0.25)	π	0.5
k_8	(0.1,0.1)	2.5π	0.2

wind and atmospheric disturbances, as well as the robustness and limitations exhibited by varying parameters of RLLP algorithms (which typically affect their attractor $I(f)$), we compare the differences in indices d and $\|\eta\|_2$ of the RLLP-sin(x) algorithm during UAV waypoint path-following. The comparisons are conducted under 6 types of wind and atmospheric disturbances (w_1 - w_6) and 8 parameter categories (k_1 - k_8), with specific parameter settings provided in Table 3 and Table 4. Experimental results are presented in Figure 20, from which the following conclusions can be drawn.

Initially, in experiments (a)-(f), as the intensity of applied steady wind speeds increases, the RLLP-sin(x) algorithm under all parameter configurations except k_5 and k_6 can maintain a desirable degree of robust stability for $\|\eta\|_2$, thereby ensuring that d achieves fast finite-time stabilization of path-following errors under disturbances. Notably, compared with other parameters, the algorithms corresponding to k_5 and k_6 overly prioritize a large exponential convergence rate $R(f)$ in the time-series curves of $\|\eta\|_2$, with the goal of confining path-following errors within the smallest possible attractor $I(f)$; consequently, they exhibit pronounced oscillatory behavior. In experiments involving stronger wind intensities (d)-(f), such detrimental impact on

stabilizing path-following errors is further amplified, rendering it evident that the corresponding index d fails to achieve strict finite-time error stabilization. This phenomenon primarily stems from the fact that an excessively large exponential convergence rate $R(f)$ exacerbates oscillations of the angle error η during convergence, thereby impairing the stabilization effect of distance errors.

Furthermore, observations of the UAV's path-following trajectories reveal that a larger attractor $I(f)$ and convergence rate $R(f)$ typically result in trajectories closer to straight lines with smaller fluctuations, enabling the UAV's actual trajectory to better evade obstacles in complex terrains. Direct evidence of this is that the trajectory corresponding to parameter k_8 exhibits a greater curvature relative to others, rendering it more susceptible to collisions with obstacles and subsequent damage. However, it possesses the advantage that the UAV's trajectory undergoes less significant variation as wind intensity increases, indicating reduced oscillations during the convergence of path-following errors—generally implying stronger adaptability of the algorithm to unknown disturbances. To quantitatively validate our assertions, we introduce the following metrics $\bar{\eta}$, η_{std} , and \bar{d} , d_{std} to characterize the error convergence performance of the time-series curves $\|\eta\|_2$ and d over the entire path-following trajectory.

$$\bar{\eta} = \frac{1}{N} \sum_{i=1}^N \|\eta(t_i)\|_2 \quad (82)$$

$$\eta_{\text{std}} = \sqrt{\frac{1}{N-1} \sum_{i=1}^N (\|\eta(t_i)\|_2 - \bar{\eta})^2} \quad (83)$$

$$\bar{d} = \frac{1}{N} \sum_{i=1}^N d(t_i) \quad (84)$$

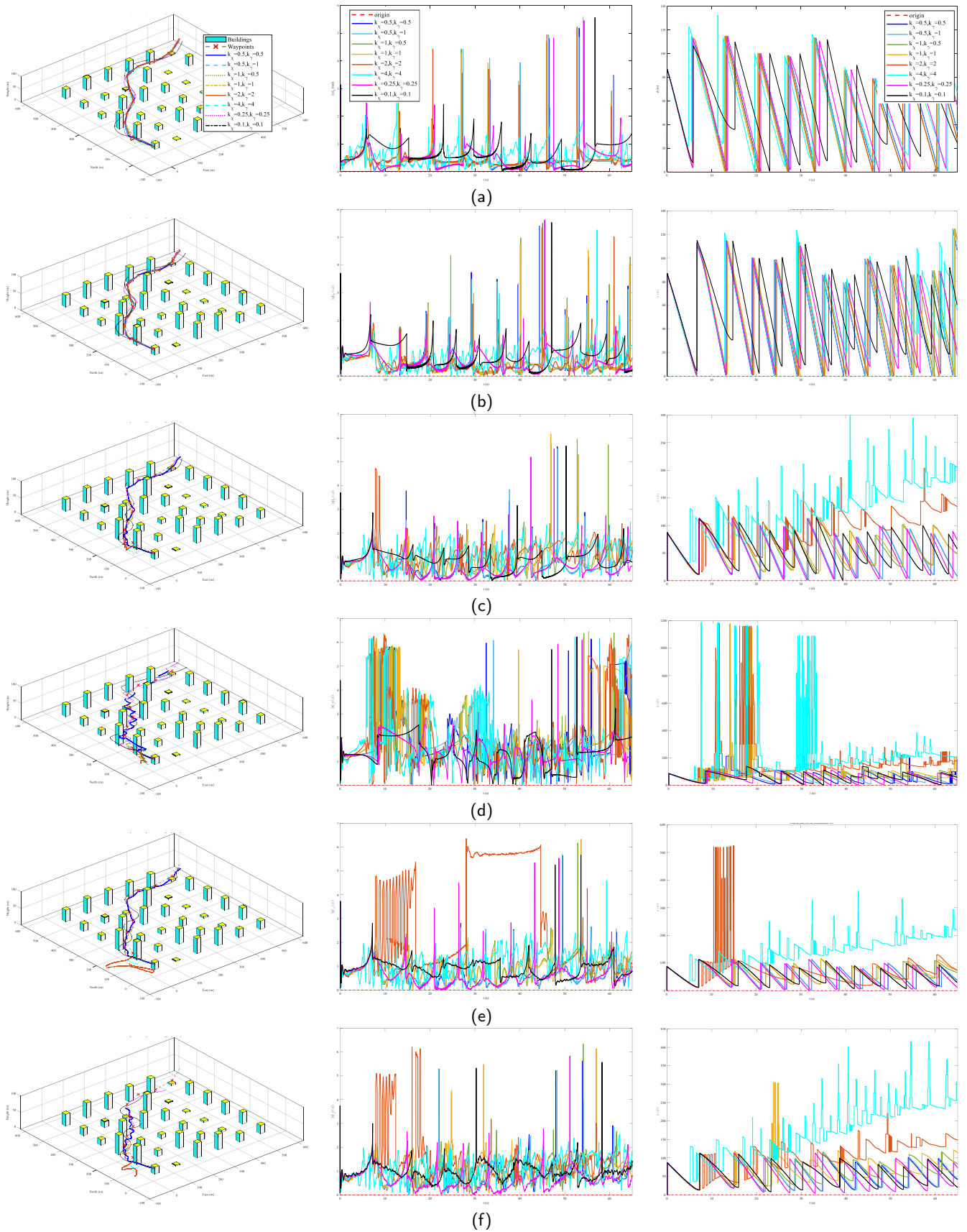


Figure 20: When different disturbances $w_1, w_2, w_3, w_4, w_5, w_6$ occur, for the conductivity RLLP-sin(x) with different parameters k_x and k_y , the path-following trajectory of the UAV for waypoints, as well as the corresponding time-series curves of d and $\|\eta\|_2$ are presented. (a): For disturbance w_1 ; (b): For disturbance w_2 ; (c): For disturbance w_3 ; (d): For disturbance w_4 ; (e): For disturbance w_5 ; (f): For disturbance w_6 .

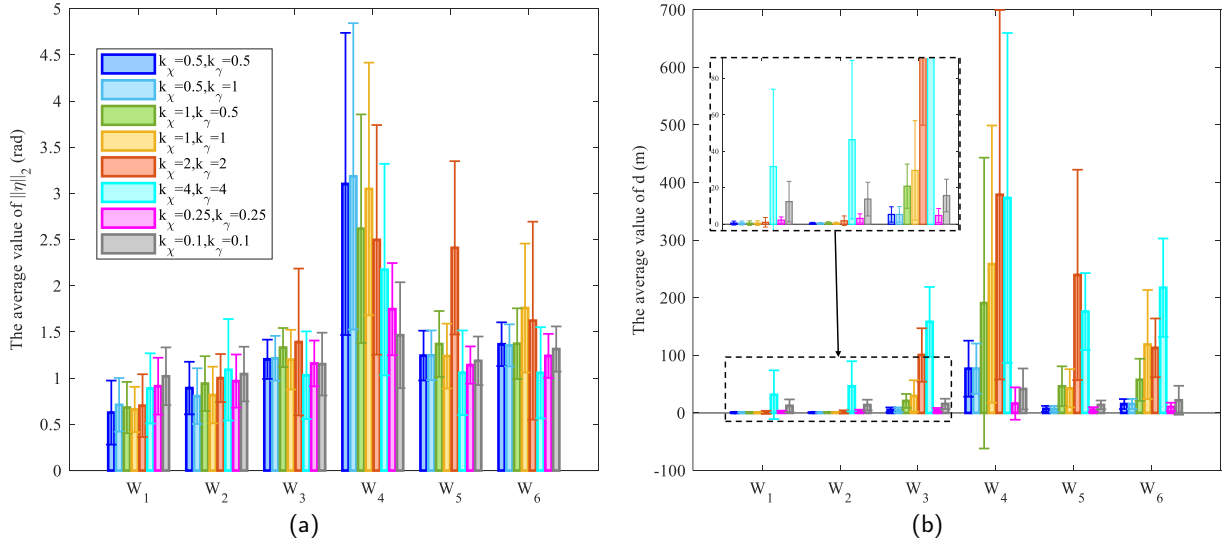


Figure 21: Comparison of indices $\bar{\eta}$ and \bar{d} during the path-following process under different disturbance conditions w_1, w_2-w_6 and different parameters k_1, k_2-k_8 . (a): The comparison on $\bar{\eta}$; (b): The comparison on \bar{d} .

$$d_{\text{std}} = \sqrt{\frac{1}{N-1} \sum_{i=1}^N (d(t_i) - \bar{d})^2} \quad (85)$$

where t_1, t_2, \dots, t_N correspond to the instants when the UAV switches the waypoints being tracked during the path-following process. Smaller magnitudes of $\bar{\eta}$ and \bar{d} signify superior error stabilization efficacy and path-following performance.

As shown in Figure 21, under disturbance conditions w_1-w_3 without random gusts, both the mean values $\bar{\eta}$ and \bar{d} of the indices, as well as their standard deviations η_{std} and d_{std} , exhibit a positive correlation with the $R(f)$ corresponding to parameter k . This trend is particularly evident when $k_\chi = k_\gamma = 2$ and $k_\chi = k_\gamma = 4$. Under disturbance conditions w_4-w_6 with random gusts applied, parameters corresponding to larger $R(f)$ (i.e., $k_\chi = k_\gamma = 4$) and those with smaller $R(f)$ (i.e., $k_\chi = k_\gamma = 0.25$) both ensure a smaller $\bar{\eta}$. However, the coefficient $k_\chi = k_\gamma = 0.25$, which corresponds to a smaller standard deviation, achieves a smaller \bar{d} and a smaller standard deviation d_{std} . This indicates that a smaller convergence rate $R(f)$ tends to guarantee a more stable anti-disturbance effect, albeit at the cost of larger trajectory curvature and partial obstacle avoidance performance. As shown in Figure 22, η_{std} exhibits a strong positive correlation with $R(f)$, which directly contributes to the positive correlation between $R(f)$ and d_{std} . This indicates that a larger $R(f)$ increases the oscillatory behavior during the convergence of η , thereby amplifying the oscillations in the convergence of distance errors. For $I(f) > 0.5$, $I(f)$ has little impact on $\bar{\eta}$ and \bar{d} . However, when $I(f) \leq 0.5$, both $\bar{\eta}$ and \bar{d} tend to decrease as $I(f)$ increases. This phenomenon is primarily attributed to the fact that a smaller $I(f)$ is typically associated with a larger $R(f)$, which leads to larger oscillation amplitudes in $\|\eta\|_2$ and d , and consequently results in larger $\bar{\eta}$ and \bar{d} .

To conclude, under strong wind disturbances, a larger attractor $I(f)$ often facilitates better finite-time robust stabilization of path-following errors. Nevertheless, a larger $I(f)$ is in many instances correlated with a larger $R(f)$. Although a larger $R(f)$ renders the waypoint-tracking trajectory closer to a straight line (aiding obstacle avoidance), it induces substantial oscillations during the convergence of path-following errors, which frequently leads to failure in stabilizing such errors. Therefore, an optimal parameter configuration principle is to constrain $I(f)$ within a small range while minimizing $R(f)$ —even though these two objectives may be mutually conflicting. This principle can, on the one hand, ensure efficient stabilization of path-following errors and avoid excessive error oscillations, and on the other hand, guarantee that the trajectory remains sufficiently close to waypoints to achieve effective obstacle avoidance.

Conclusions and future work

In summary, the innovative aspects of our work are summarized as follows:

(1) From the perspective of global random attractors, we propose a novel approach to determine the exponential convergence of perturbed nonlinear systems (see Theorem 1), thereby introducing the metrics $R(f)$ and $I(f)$ to quantify the exponential convergence rate and the range of the ultimate convergence set, respectively. Additionally, we establish the sufficient conditions for the look-ahead pursuit guidance law to achieve rapid finite-time stability (see Theorem 3);

(2) Building upon the aforementioned theoretical framework, we develop a robust longitudinal-lateral look-ahead pursuit (RLLP) guidance method based on the traditional longitudinal and lateral look-ahead pursuit approach (see Eq. (46)). We further quantify the key metrics characterizing its

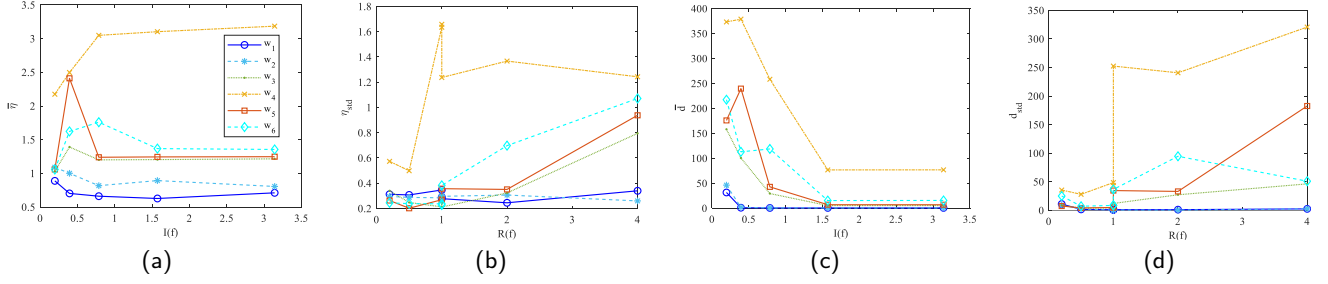


Figure 22: The statistical analysis based on the results in Figure 21 reveals the effects of RLLP-sin(x) under different $I(f)$ and $R(f)$ (corresponding to parameters k_1 - k_8) on the metrics $\tilde{\eta}$, η_{std} , \tilde{d} , and d_{std} under various disturbances w_1 - w_6 . (a): Impact of $I(f)$ on $\tilde{\eta}$; (b): Impact of $R(f)$ on η_{std} ; (c): Impact of $I(f)$ on \tilde{d} ; (d): Impact of $R(f)$ on d_{std} .

robustness and propose a method to optimize these robustness metrics (see Algorithm 1);

(3) Using real obstacle environments, UAV dynamics, and aerodynamic models, we validate the effectiveness, optimality, and robustness of the proposed RLLP guidance algorithm against realistic atmospheric disturbances through simulation experiments. Finally, we discuss the principles for adjusting guidance parameters in more complex environments and under wind field perturbations.

Future research will focus on refining these principles, specifically involving the rational design of the guidance function f to minimize $R(f)$ while confining $I(f)$ within a specified range, thereby ensuring smooth convergence of path-following errors.

Acknowledgements

This work was supported by the National Natural Science Foundation of China (No.51775435). The preprint version is available at: <https://arxiv.org/abs/2505.16407>.

References

- [1] Wei Wang, Chao Fang, and Ting Liu. Multiperiod unmanned aerial vehicles path planning with dynamic emergency priorities for geohazards monitoring. *IEEE TRANSACTIONS ON INDUSTRIAL INFORMATICS*, 18(12):8851–8859, DEC 2022.
- [2] Lasse Frigstad, Vegard Furu, Sigve Kristiansen Svenkerud, Andreas Claesson, Henrik Andersson, and Tobias Andersson Granberg. Joint planning of drones and volunteers in emergency response to out-of-hospital cardiac arrest. *COMPUTERS & INDUSTRIAL ENGINEERING*, 185, NOV 2023.
- [3] Mingqiu Ren, Bingqie Wang, and Yi Leng. Research on multi domain joint reconnaissance of uva swarm. In *International Conference on Guidance, Navigation and Control*, pages 12–18. Springer, 2024.
- [4] A Pedro Aguiar and Joao P Hespanha. Trajectory-tracking and path-following of underactuated autonomous vehicles with parametric modeling uncertainty. *IEEE transactions on automatic control*, 52(8):1362–1379, 2007.
- [5] A Pedro Aguiar, Joao P Hespanha, and Petar V Kokotović. Performance limitations in reference tracking and path following for nonlinear systems. *Automatica*, 44(3):598–610, 2008.
- [6] PB Sujit, Srikanth Saripalli, and Joao Borges Sousa. Unmanned aerial vehicle path following: A survey and analysis of algorithms for fixed-wing unmanned aerial vehicles. *IEEE Control Systems Magazine*, 34(1):42–59, 2014.
- [7] Saurabh Kumar, Shashi Ranjan Kumar, and Abhinav Sinha. Robust path-following guidance for an unmanned vehicle. In *AIAA SCITECH 2023 Forum*, page 1055, 2023.
- [8] Praveen Kumar Ranjan, Abhinav Sinha, and Yongcan Cao. Robust uav guidance law for safe target circumnavigation with limited information and autopilot lag considerations. In *AIAA SCITECH 2024 Forum*, page 0124, 2024.
- [9] Saurabh Kumar, Shashi Ranjan Kumar, and Abhinav Sinha. Three-dimensional path-following nonlinear guidance for unmanned aerial vehicles. *Journal of Guidance, Control, and Dynamics*, 47(6):1231–1240, 2024.
- [10] Isaac Kaminer, António Pascoal, Enric Xargay, Naira Hovakimyan, Chengyu Cao, and Vladimir Dobrokhodov. Path following for small unmanned aerial vehicles using 11 adaptive augmentation of commercial autopilots. *Journal of guidance, control, and dynamics*, 33(2):550–564, 2010.
- [11] Patrick Piprek, Haichao Hong, and Florian Holzapfel. Optimal trajectory design accounting for robust stability of path-following controller. *Journal of Guidance, Control, and Dynamics*, 45(8):1385–1398, 2022.
- [12] Takeshi Yamasaki, SN Balakrishnan, and Hiroyuki Takano. Separate-channel integrated guidance and autopilot for automatic path-following. *Journal of Guidance, Control, and Dynamics*, 36(1):25–34, 2013.
- [13] Ahmed S Rezk, Horacio M Calderón, Herbert Werner, Benjamin Herrmann, and Frank Thielecke. Predictive path following control for fixed wing uavs using the qlmpc framework in the presence of wind disturbances. In *AIAA SCITECH 2024 Forum*, page 1594, 2024.
- [14] Jun Yang, Cunjia Liu, Matthew Coombes, Yunda Yan, and Wen-Hua Chen. Optimal path following for small fixed-wing uavs under wind disturbances. *IEEE Transactions on Control Systems Technology*, 29(3):996–1008, 2020.
- [15] Weijia Yao, Héctor Garcia de Marina, Bohuan Lin, and Ming Cao. Singularity-free guiding vector field for robot navigation. *IEEE Transactions on Robotics*, 37(4):1206–1221, 2021.
- [16] Weijia Yao. Path following control in 3d using a vector field. In *Guiding Vector Fields for Robot Motion Control*, pages 39–62. Springer, 2023.
- [17] Zian Wang, Zheng Gong, Jinfa Xu, Jin Wu, and Ming Liu. Path following for unmanned combat aerial vehicles using three-dimensional nonlinear guidance. *IEEE-ASME TRANSACTIONS ON MECHATRONICS*, 27(5):2646–2656, OCT 2022.
- [18] Saurabh Kumar, Abhinav Sinha, and Shashi Ranjan Kumar. Robust path-following guidance for an autonomous vehicle in the presence of wind. *AEROSPACE SCIENCE AND TECHNOLOGY*, 150, JUL 2024.
- [19] Randal W Beard, Jeff Ferrin, and Jeffrey Humpherys. Fixed wing uav path following in wind with input constraints. *IEEE Transactions on Control Systems Technology*, 22(6):2103–2117, 2014.
- [20] Thomas Stastny. L1 guidance logic extension for small uavs: handling high winds and small loiter radii. *arXiv preprint arXiv:1804.04209*,

2018.

- [21] Cunjia Liu, Owen McAree, and Wen-Hua Chen. Path-following control for small fixed-wing unmanned aerial vehicles under wind disturbances. *International Journal of Robust and Nonlinear Control*, 23(15):1682–1698, 2013.
- [22] Toufik Souanef. \mathcal{L}_1 adaptive path-following of small fixed-wing unmanned aerial vehicles in wind. *IEEE Transactions on Aerospace and Electronic Systems*, 58(4):3708–3716, 2022.
- [23] Weinan Wu, Yao Wang, Chunlin Gong, and Dan Ma. Path following control for miniature fixed-wing unmanned aerial vehicles under uncertainties and disturbances: a two-layered framework. *NONLINEAR DYNAMICS*, 108(4):3761–3781, JUN 2022.
- [24] AJ Van Schaft. l_2 -gain analysis of nonlinear systems and nonlinear state-feedback h_∞ control. *IEEE Trans. Autom. Control*, 37(6):770–784, 1992.
- [25] Suiyang Khoo, Lihua Xie, Shengkui Zhao, and Zhihong Man. Multi-surface sliding control for fast finite-time leader–follower consensus with high order siso uncertain nonlinear agents. *International Journal of Robust and Nonlinear Control*, 24(16):2388–2404, 2014.
- [26] Martin Burston, Roberto Sabatini, Alessandro Gardi, and Reece Clothier. Reverse engineering of a fixed wing unmanned aircraft 6-dof model based on laser scanner measurements. In *2014 IEEE Metrology for Aerospace (MetroAeroSpace)*, pages 144–149. IEEE, 2014.
- [27] Randal W Beard and Timothy W McLain. *Small unmanned aircraft: Theory and practice*. Princeton university press, 2012.
- [28] Robert F Stengel. *Flight dynamics*. Princeton university press, 2005.
- [29] Jack W Langelaan, Nicholas Alley, and James Neidhoefer. Wind field estimation for small unmanned aerial vehicles. *Journal of guidance, control, and dynamics*, 34(4):1016–1030, 2011.